



HAL
open science

Description of Martian Convective Vortices Observed by InSight and Implications for Vertical Vortex Structure and Subsurface Physical Properties

Keisuke Onodera, Kiwamu Nishida, Taichi Kawamura, Naomi Murdoch, Mélanie Drilleau, Ryoji Otsuka, Ralph Lorenz, Anna Horleston, Rudolf Widmer-Schmidrig, Martin Schimmel, et al.

► To cite this version:

Keisuke Onodera, Kiwamu Nishida, Taichi Kawamura, Naomi Murdoch, Mélanie Drilleau, et al.. Description of Martian Convective Vortices Observed by InSight and Implications for Vertical Vortex Structure and Subsurface Physical Properties. *Journal of Geophysical Research. Planets*, 2023, 128 (8), pp.e2023JE007896. 10.1029/2023JE007896 . hal-04184039

HAL Id: hal-04184039

<https://hal.science/hal-04184039>

Submitted on 21 Aug 2023

HAL is a multi-disciplinary open access archive for the deposit and dissemination of scientific research documents, whether they are published or not. The documents may come from teaching and research institutions in France or abroad, or from public or private research centers.

L'archive ouverte pluridisciplinaire **HAL**, est destinée au dépôt et à la diffusion de documents scientifiques de niveau recherche, publiés ou non, émanant des établissements d'enseignement et de recherche français ou étrangers, des laboratoires publics ou privés.



Distributed under a Creative Commons Attribution - NonCommercial - NoDerivatives 4.0 International License

Description of Martian Convective Vortices Observed by InSight and Implications for Vertical Vortex Structure and Subsurface Physical Properties



Key Points:

- We quantitatively characterized the Martian convective vortices observed by InSight's seismometer and meteorological instruments
- Focusing on the pressure drop profiles, we inferred a link between the asymmetry and the vertical vortex structure
- With the cataloged parameters, we performed a compliance analysis and evaluated the ground rigidity at the InSight landing site
















Correspondence to:

K. Onodera,
onodera@eri.u-tokyo.ac.jp

Citation:

Onodera, K., Nishida, K., Kawamura, T., Murdoch, N., Drilleau, M., Otsuka, R., et al. (2023). Description of Martian convective vortices observed by InSight and implications for vertical vortex structure and subsurface physical properties. *Journal of Geophysical Research: Planets*, 128, e2023JE007896. <https://doi.org/10.1029/2023JE007896>

Received 18 MAY 2023
 Accepted 4 AUG 2023

Keisuke Onodera¹ , Kiwamu Nishida¹ , Taichi Kawamura² , Naomi Murdoch³ , Mélanie Drilleau³ , Ryoji Otsuka^{4,5}, Ralph Lorenz⁶ , Anna Horleston⁷ , Rudolf Widmer-Schmidrig⁸, Martin Schimmel⁹ , Sebastien Rodriguez² , Sebastián Carrasco¹⁰ , Satoshi Tanaka^{4,5}, Clement Perrin¹¹ , Philippe Lognonné² , Aymeric Spiga¹² , Don Banfield¹³, Mark Panning¹⁴ , and William Bruce Banerdt¹⁴ 

¹Earthquake Research Institute, The University of Tokyo, Tokyo, Japan, ²Université Paris Cité, Institut de Physique du Globe de Paris, CNRS, Paris, France, ³Institut Supérieur de l'Aéronautique et de l'Espace (ISAE-SUPAERO), Université de Toulouse, Toulouse, France, ⁴Department of Complexity Science and Engineering, The University of Tokyo, Chiba, Japan, ⁵Institute of Space and Astronautical Science, Japan Aerospace Exploration Agency, Tokyo, Japan, ⁶Johns Hopkins University Applied Physics Laboratory, Laurel, MD, USA, ⁷School of Earth Sciences, University of Bristol, Bristol, UK, ⁸Black Forest Observatory, Wolfach, Germany, ⁹Geociencias Barcelona, Barcelona, Spain, ¹⁰Bensberg Observatory, University of Cologne, Bergisch Gladbach, Germany, ¹¹Nantes Université, Université d'Angers, Le Mans Université, CNRS, UMR 6112, Laboratoire de Planétologie et Géosciences, UAR 3281, Observatoire des Sciences de l'Univers de Nantes Atlantique, Nantes, France, ¹²Laboratoire de Météorologie Dynamique/Institut Pierre-Simon Laplace (LMD/IPSL), Centre National de la Recherche Scientifique (CNRS), Sorbonne Université, Paris, France, ¹³Cornell Center for Astrophysics and Planetary Science, Cornell University, Ithaca, NY, USA, ¹⁴Jet Propulsion Laboratory, California Institute of Technology, Pasadena, CA, USA

Abstract Convective vortices (whirlwinds) and dust devils (dust-loaded vortices) are one of the most common phenomena on Mars. They reflect the local thermodynamical structure of the atmosphere and are the driving force of the dust cycle. Additionally, they cause an elastic ground deformation, which is useful for retrieving the subsurface rigidity. Therefore, investigating convective vortices with the right instrumentation can lead to a better understanding of the Martian atmospheric structures as well as the subsurface physical properties. In this study, we quantitatively characterized the convective vortices detected by NASA's InSight (~13,000 events) using meteorological (e.g., pressure, wind speed, temperature) and seismic data. The evaluated parameters, such as the signal-to-noise ratio, event duration, asymmetry of pressure drop profiles, and cross-correlation between seismic and pressure signals, are compiled as a catalog. Using these parameters, we investigated (a) the vortex structure and (b) the subsurface physical properties. Regarding the first topic, we tried to illustrate the vertical vortex structure and its link to the shape of the pressure profiles by combining the asymmetrical features seen in the observed pressure drops and the terrestrial observations of dust devils. Our results indicate that most of the vortices move with the wall tilted in the advection direction. Concerning the second topic, selecting the highly correlated events between pressure perturbation and ground response, we estimated the subsurface rigidity at the InSight landing site down to 100 m depth. Our results indicate that the subsurface structure can be modeled with two layers having a transition at 5–15 m depth.

Plain Language Summary As frequently observed on Earth, convective vortices or dust-loaded vortices are also seen on Mars. They reflect the local atmospheric structure and are the main driving force to lift the fine dust from the ground. In 2018, NASA's InSight succeeded in installing the meteorological and geophysical packages on Mars. That brought us, in particular, meteorological data with an extremely high temporal resolution, contributing to resolving local phenomena such as convective vortices. In this study, using InSight's meteorological (e.g., pressure, air temperature) and seismic data, we quantitatively characterize convective vortices to understand this phenomenon from both meteorological and geophysical aspects. Especially focusing on the asymmetry of pressure drop profiles at vortex encounters and the correlation between the pressure variations and seismic signals, we investigated (a) a link between the shape of pressure drop profiles and the vertical vortex structure and (b) the ground rigidity structure by measuring the ground responses against the vortex-related pressure variations. Consequently, first, we found that most of the vortices move with the wall tilted in the advection direction. Second, our results indicated that the subsurface structure can be modeled with two layers down to 100 m with a transition at 5–15 m depth.

© 2023. The Authors.

This is an open access article under the terms of the [Creative Commons Attribution-NonCommercial-NoDerivs License](https://creativecommons.org/licenses/by/4.0/), which permits use and distribution in any medium, provided the original work is properly cited, the use is non-commercial and no modifications or adaptations are made.

1. Introduction

NASA's Interior Exploration using Seismic Investigations, Geodesy and Heat Transport (InSight) was operated on Mars from November 2018 to December 2022, conducting quasi-continuous seismic and meteorological observations. These observations produced many discoveries and made significant progress in Martian science, such as the detection of marsquakes (e.g., Banerdt et al., 2020; Ceylan et al., 2021; Clinton et al., 2021; Giardini et al., 2020), revealing the internal structure (e.g., Irving et al., 2023; Khan et al., 2021; Knapmeyer-Endrun et al., 2021; Lognonné et al., 2020; Stähler et al., 2021), and new insights into atmospheric activities (e.g., Banfield et al., 2020; Spiga et al., 2021).

In this study, we pay special attention to the convective vortices or dust devils, which are one of the most common atmospheric phenomena on Mars (e.g., Ellehoj et al., 2010; Martínez et al., 2017; Murphy & Nelli, 2002; Reiss et al., 2014; Ryan & Lucich, 1983). The quasi-continuous and high temporal resolution data from InSight plays an important role in improving our knowledge of the local-scale meteorological phenomena on Mars (e.g., Banfield et al., 2020; Martínez et al., 2017; Spiga et al., 2018, 2021).

As convective vortices strongly reflect the thermodynamical structure of the local atmosphere, they are useful to capture near-surface atmospheric activities. Also, convective vortices with dust lifting (i.e., dust devils) are a pivotal mechanism of the transportation of dust particles from the ground to the atmosphere (e.g., Balme & Greeley, 2006; Bila et al., 2020; Kahre et al., 2017). Another important aspect of the convective vortex is the coupling with the ground (atmosphere-ground interaction). The elastic ground deformation related to pressure perturbations has been observed on Earth (e.g., Sorrells, 1971; Sorrells & Goforth, 1973; Sorrells et al., 1971), including the specific case of dust devils (Lorenz et al., 2015). The vortex-generated ground deformation was expected to also occur on Mars (e.g., Kenda et al., 2017; Murdoch et al., 2017). Owing to the simultaneous observations of the seismometer and barometer of the InSight mission (e.g., Banerdt et al., 2020), the same phenomenon was also detected on Mars. That allowed us to investigate the subsurface rigidity by measuring the ground deformations caused by transient atmospheric pressure variations (so-called "compliance") (e.g., Banerdt et al., 2020; Kenda et al., 2020; Lognonné et al., 2020; Murdoch et al., 2021). Therefore, studying the convective vortex or dust devil is important to push forward our understanding of Martian meteorology, subsurface geology, and atmosphere-ground interactions.

The InSight observations up to Sol 900 (a Sol is a Martian day) brought us about 13,000 pressure drop events (see Spiga et al. (2021) for the details of the detection algorithm). Based on the pressure profile features observed both on Earth and Mars (e.g., sudden pressure drops with amplitudes of 0.1–10 Pa and event duration of several seconds to several tens of seconds), these events are considered to be convective vortices (Chatain et al., 2021; Lorenz et al., 2021; Murphy et al., 2016; Spiga et al., 2021). The initial description of some of these observations has been summarized by Banfield et al. (2020) (~Sol 200) and Spiga et al. (2021) (~Sol 400) from a meteorological point of view and by Lorenz et al. (2021) (~Sol 400) focusing on both meteorological and seismic observations. The motivation of this study is to give a description of all the detected pressure drop events up to Sol 900 and to provide constructive information for future studies on the Martian convective vortices. Additionally, with larger data sets than before, we will perform compliance analysis to update the subsurface rigidity model at the InSight landing site.

In this paper, accompanied by an introduction of InSight's scientific instruments, we present a general summary of the convective vortices observed by InSight. Then, we describe how to characterize the observed convective vortices in a quantitative way. In addition to the meteorological aspect, by computing the cross-correlation between the pressure and seismic data, we also discuss the atmosphere-ground interaction. In the end, we provide two examples of the application of our catalog to the scientific discussion: (a) the relation between vortex structure and asymmetry of pressure drop profile and (b) the subsurface rigidity derived through the analysis of the ground deformation caused by temporal pressure variations (compliance).

2. Overview of the InSight Seismic and Meteorological Packages

In this study, we used the seismic and meteorological data recorded by InSight's scientific instruments. This section summarizes the fundamental information of each instrument and specification. A thorough description

of the seismometers and the meteorological package can be found in Lognonné et al. (2019) and Banfield et al. (2018).

2.1. Seismometers

The ground vibrations (e.g., due to quakes, environmental noises, and meteoroid impacts) are measured with the Seismic Experiment for Interior Structure (SEIS, Lognonné et al., 2019), which consists of six seismometers. Three are the Very Broad-Band (VBB) seismometers installed obliquely (dip angle is about -29.5° with 120° azimuthal difference between each sensor) and the other three are Short Period seismometers having one vertical and two horizontal components. As this study uses only the VBB data, here we focus on the specification of VBB.

The VBB sensor shows an almost flat response between 0.05 and 15 Hz and nominally samples the data at 20 samples per second (sps). Covered with the Wind and Thermal Shield, the seismic recordings from Mars showed a noise level of 1.5×10^{-10} m/s²/Hz^{0.5} at quiet nighttime and a few times 10^{-8} m/s²/Hz^{0.5} during the windy daytime (e.g., Lognonné et al., 2020, 2023). Generally, the VBB data are distributed with the unit of DU (i.e., the instrumental response is not decomposed), and also the rotation from the oblique axis system (UVW components) into the north, east, and vertical system (NEZ components) is not performed. In the following analysis, we use the NEZ velocity or acceleration data obtained by performing the deconvolution of the instrumental response and the rotation from UVW to NEZ components. A sample program for this processing is provided by Onodera (2023b).

2.2. Pressure Sensor

The atmospheric pressure is measured by Pressure Sensor (PS) included in the Auxiliary Payload Sensor Suite (APSS, Banfield et al., 2018), which is located near the center of the lander platform. The PS is composed of a pressure transducer, a Quad-Disk type inlet system, and a tube connecting the former two components (Banfield et al., 2018). The transducer records the pressure variations as an electrical signal, and the signal is converted into Pascals taking into account the sensor's temperature. The detailed processing and the background physics are well described by Banfield et al. (2018), Banfield (2019), and Rodriguez-Manfredi (2019). The pressure signals are nominally recorded at 10 Hz (or sps). The noise level at the InSight landing site is about 10 mPa/Hz^{0.5} from 0.1 to 1 Hz and 50 mPa/Hz^{0.5} at 0.01 Hz (e.g., Banfield et al., 2020; Spiga et al., 2021). In the analysis, we use the calibrated PS data (i.e., the data converted into Pascals).

2.3. Temperature and Wind Sensors

The air temperature, wind speed, and wind direction are evaluated with the data from Temperature and Wind Sensors for InSight (TWINS; Banfield et al., 2018) included in the APSS. The two TWINS booms face west and east and are mounted at 121.5 and 111.5 cm altitude, due to the tilt of the lander (Banfield et al., 2020; Spiga et al., 2021). Each boom includes three hot-film anemometers for estimating the wind speed and direction (Banfield et al., 2018). The idea of the wind measurement is to monitor the amount of power supplied to keep the sensors' temperature constant while the sensors are exposed to the air and cooled down by the ambient wind. Full use of the data from three anemometers (i.e., 3-D wind sensor) on each boom enables us to reconstruct the local wind field, eventually giving us the wind speed and direction (see Banfield et al. (2018) for the details). This study uses the calibrated data (i.e., the data converted into m/s for wind speed and N°E for wind direction).

The air temperature is computed based on the recordings by Atmospheric Temperature Sensor (ATS) attached to the base of the respective TWINS booms. There are three thermistors bonded to the 35 mm long ATS rod that monitor the change in electrical resistivity due to the surrounding temperature variations (Banfield et al., 2018). The conversion of the raw ATS data into the temperature is performed considering the thermal balance between a thin rod and the surrounding fluid (Mueller & Abu-Mulaweh, 2006; Zorzano et al., 2009). In the analysis, we use the calibrated data (i.e., the data already converted into Kelvins), which is generally retrievable from open archives.

As described by Banfield et al. (2018) and Spiga et al. (2021), the accuracy for the measurements are 1 m/s (wind speed), 22.5° (wind direction), and 5 K (air temperature), respectively. It is noteworthy that the saturation of the

Table 1
Channel Names for Respective Instruments

Instrument	Sampling rate (sps)	Unit	Channel name	
Seismometer	20	Digital unit	XB.ELYSE.02.BHU	
			XB.ELYSE.02.BHV	
			XB.ELYSE.02.BHW	
Pressure sensor	10	Pa	XB.ELYSE.13.BDO	
Wind sensor (direction)	0.1	N°E	XB.ELYSE.33.VWD	
			0.5	XB.ELYSE.30.VWD
			1.0	XB.ELYSE.30.LWD
Wind sensor (speed)	0.1	m/s	XB.ELYSE.33.VWS	
			0.5	XB.ELYSE.30.VWS
			1.0	XB.ELYSE.30.LWS
Air temperature	0.1	K	XB.ELYSE.33.VKO	
			0.5	XB.ELYSE.30.VKO
			1.0	XB.ELYSE.30.LKO

Note. Readers may refer to Onodera (2023b) for removing the instrumental response from the raw seismic data (i.e., converting the digital unit) into a physical unit such as m/s.

wind speed sensor occurs above 20 m/s, and that the measurements become unreliable when the wind speed is smaller than 2.8 m/s.

2.4. Channels Used for the Analysis

In the following analyses, we basically use the seismic and pressure data sampled at the nominal sampling rate—10 sps for pressure data and 20 sps for seismic data, respectively. Concerning the wind speed, wind direction, and air temperature data, we made use of 0.1, 0.5, or 1.0 sps data as long as either of them is available. The channel names for respective data, which can be used to retrieve the original data from the public archive system such as Planetary Data System (PDS), are shown in Table 1.

3. Temporal Distribution and Size-Frequency Distribution of the Observed Convective Vortices

Figure 1a shows the temporal distribution of the convective vortices detected with the algorithm proposed by Spiga et al. (2021). The time evolution of atmospheric pressure, air temperature, wind speed, and wind direction are also shown for comparison in Figures 2a–2d, where the blank areas correspond to the periods of the conjunction or times when the respective instruments were turned off. Based on both observations and numerical simulations, it is considered that convective vortices are formed mostly when the atmosphere becomes convective and turbulent in the daytime due to the heat input by the Sun on the surface. Almost all the vortices have been

observed during the daytime at the InSight landing site (Figures 1a and 1c), when there is a strong temperature gradient between the Martian ground and the atmosphere. Generally, the vortices were detected between 9 and 16 hr in Local True Solar Time (LTST) when the atmospheric turbulence was vigorous, which can be seen as the atmospheric pressure decrease, the air temperature increase, and the increase in the wind speed (Figures 2a–2c). Regarding the seasonal variations (Figure 1b), we observe the annual tendency that the event number increases

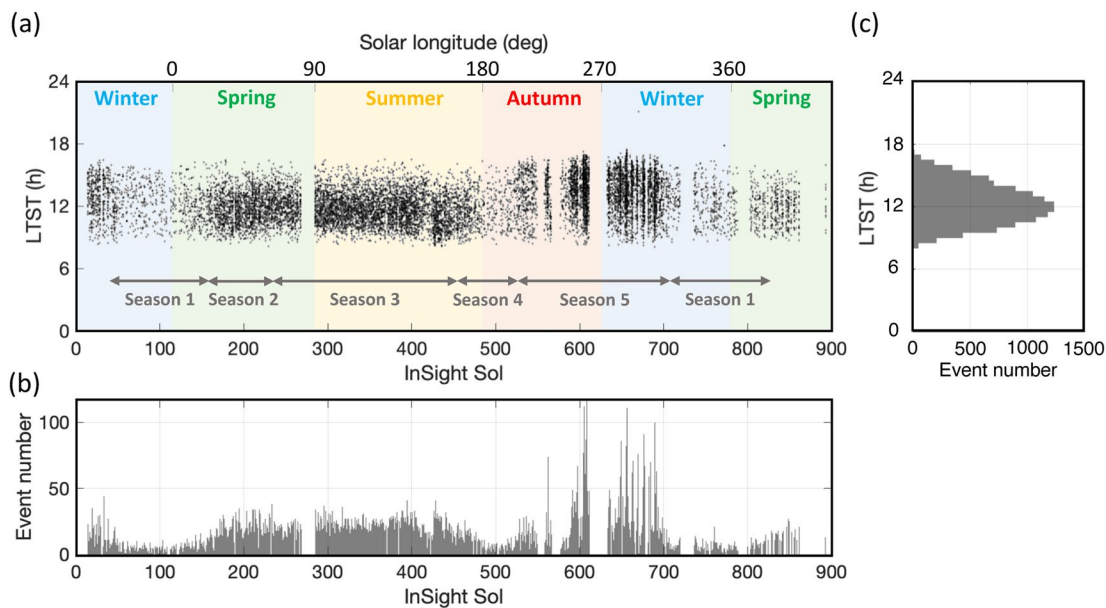


Figure 1. (a) Temporal distribution of the detected convective vortices. Each black point shows a detected vortex. The vertical axis shows the Local True Solar Time, the bottom horizontal axis shows the InSight sol and the top horizontal axis shows the solar longitude. The different background color indicates different seasons. In addition to ordinarily used seasons, we show “Seasons 1–5” proposed by Chatain et al. (2021) based on turbulence tendency over a Martian year. (b) Histogram of the detected events per sol. (c) Histogram of the detected events for every hour.

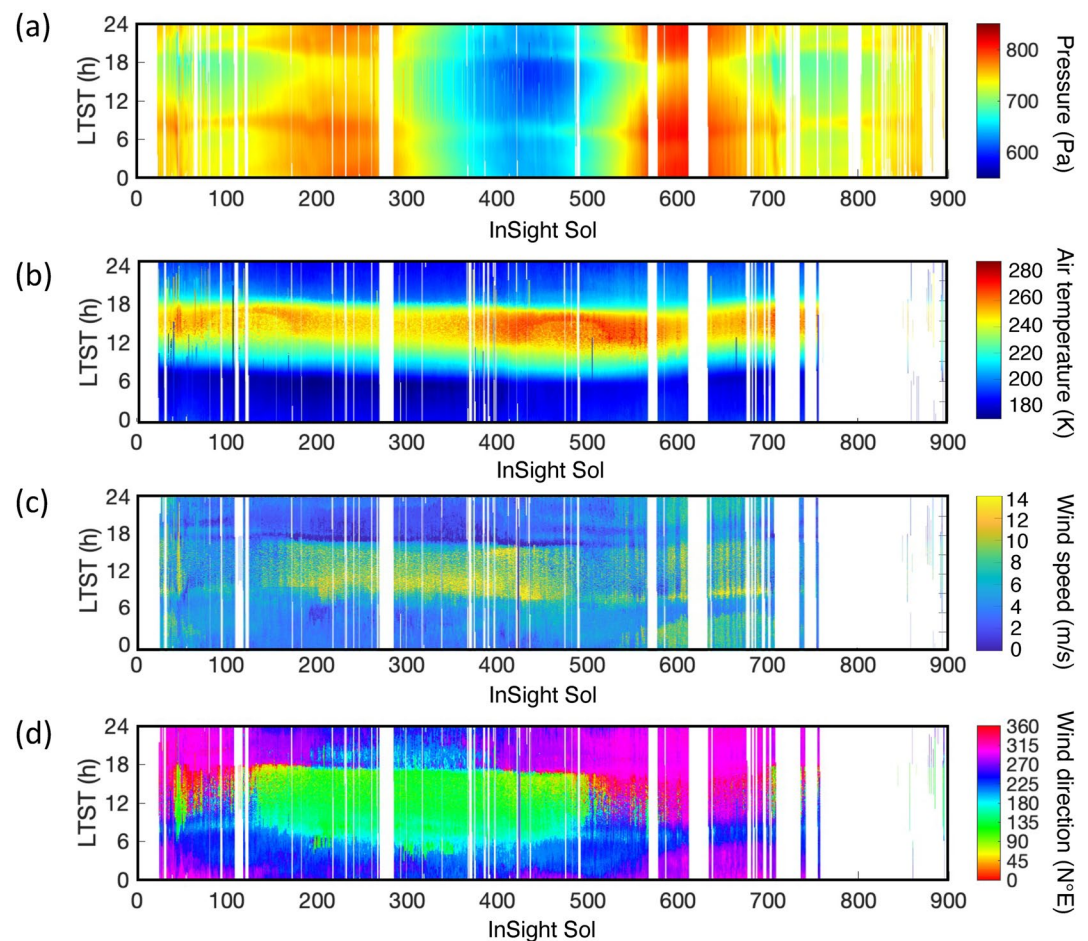


Figure 2. Diurnal and seasonal variations of (a) atmospheric pressure, (b) air temperature, (c) wind speed, and (d) wind direction.

from winter to spring, is relatively stable during summer, decreases at the beginning of autumn, and then spikes at the transition from autumn to winter. Chatain et al. (2021) investigated the seasonal variations in local turbulence and defined five seasons (Season 1–5) besides normally used ones. According to their results, the Martian atmosphere gets turbulent in Season 5, which is confirmed as the rapid increase in the number of vortices. See Chatain et al. (2021) for details about the seasonal variations of the Martian atmospheric activity.

There are a smaller number of detections of pressure drops at night (Figures 1a and 1c), consistent with past missions (Phoenix and Curiosity) that have also observed occasional night-time pressure drops (e.g., Ellehoj et al., 2010; Ordonez-Etxeberria et al., 2018). Ellehoj et al. (2010) interpreted that these events were caused by the interaction of the atmosphere and the local topography, and the observations by other missions support this idea. For example, many night-time events were confirmed at Gale crater (the Curiosity landing site) which has a complex local topography (e.g., Ordonez-Etxeberria et al., 2018). On the contrary, few night-time events were observed at the landing site of Mars Pathfinder, where the topography is relatively smooth and flat (e.g., Kahanpää et al., 2016). Since the InSight landing site is also smooth and flat (e.g., Golombek et al., 2017; Golombek et al., 2020), a small number of detections of night-time events (Chatain et al., 2021) appear consistent with this past interpretation.

Figure 3 summarizes the cumulative size-frequency distribution (CSFD) of pressure drops observed by the past and ongoing missions carrying a barometer (i.e., Mars Pathfinder, Phoenix, Curiosity, InSight, and Perseverance; Banfield et al., 2018; Ellehoj et al., 2010; Hueso et al., 2023; Murphy & Nelli, 2002; Ordonez-Etxeberria et al., 2018). The CSFD data for Mars Pathfinder, Phoenix, Curiosity, and Perseverance were retrieved from previous works (Ellehoj et al., 2010; Hueso et al., 2023; Murphy & Nelli, 2002; Ordonez-Etxeberria et al., 2018), and

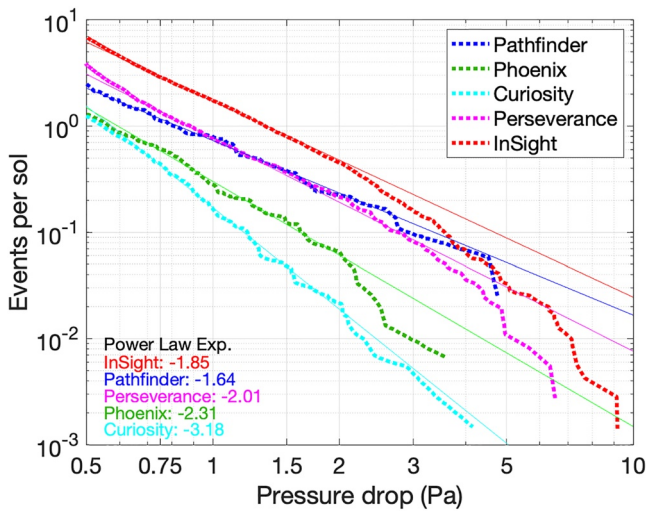


Figure 3. Comparison of the cumulative size-frequency distribution of pressure drops per sol for the past and ongoing Mars missions corrected for observation time bias (dotted profiles). The solid lines represent the fitted curves between 0.65 and 1.8 Pa with a power law. The exponents are shown in the bottom legend.

then the power-law fitting was performed using the data between 0.65 and 1.8 Pa (Figure 3). Following the idea of Ordóñez-Etxebarria et al. (2018), the cumulative number is corrected to “events per sol” because the observation period differs from mission to mission, which allows us to perform a direct comparison. Interestingly, comparing InSight’s CSFD with those of other missions, InSight detected more events than any other missions (Figure 3), which is in agreement with Spiga et al. (2021) and Newman et al. (2022) and contrary to what was presented by Jackson (2022). The InSight’s CSFD at smaller pressure drops (<1.8 Pa) can be fitted with a power law with a -2 slope, which is consistent with others except for Curiosity (slope is -3). The discrepancy between Curiosity’s observations with others has been explained by the effect of the shorter Planetary Boundary Layer (PBL) within Gale crater (~ 2 km) compared to the outside of the crater (8–10 km) (Ordóñez-Etxebarria et al., 2018) or other landing sites (e.g., 5–8 km at InSight landing site; Spiga et al., 2021). When the PBL gets shorter, it becomes more difficult to develop convective vortices in the same way as at the other landing sites, resulting in the lack of larger pressure drop events (>1 –2 Pa). Looking at those CSFDs with a slope of -2 , we found a kink where the profile starts to be off the trend. Building on the discussion by Ordóñez-Etxebarria et al. (2018), this cut-off pressure value might be determined by the PBL height at each landing site. Since recent missions such as InSight and Perseverance provide us with continuous meteorological recordings with high-temporal resolution (1 Hz for Perseverance and 10 Hz for InSight), future studies could deepen this topic by making the best of these two missions’ data.

4. Data Set

We focus on the 12,569 convective vortices detected with the same method used by previous studies (e.g., Chatain et al., 2021; Spiga et al., 2021). The event list can be found at Onodera (2023a), where the events’ occurrence time in both UTC and Sol with local time, and the maximum (negative) amplitude of the pressure drop are summarized. This study covers the observation period up to Sol 900 during which the pressure data was quasi-continuously recorded. After that time, the pressure and wind data are recorded so sparsely that few events are recorded, and correcting for sampling biases becomes difficult. For every detected event, we cut out the 20 min time traces centered at the maximum pressure drop for seismic (velocity and acceleration data) and meteorological data (pressure, wind speed, wind direction, and air temperature) if each data were recorded.

5. Parameters Retrieved From the Convective Vortices Observed by InSight

5.1. Signal-To-Noise Ratio of Ground Acceleration and Air Pressure

The signal-to-noise ratio (SNR) is a useful parameter to judge the data quality, and we calculated it for the time series recorded by VBB and PS at various frequency bands. The frequency bands are defined as follows: Band 1 (0.01–0.05 Hz), Band 2 (0.05–0.1 Hz), Band 3 (0.1–0.5 Hz), Band 4 (0.5–1.0 Hz), and Band 5 (1.0–2.0 Hz). In the respective frequency bands, the SNR was estimated by taking the ratio of the peak signal amplitude due to the encounter of a vortex over the background noise signal, that is:

$$SNR = \frac{S_{peak}}{S_{noise}}, \quad (1)$$

where S_{peak} is the absolute value of the peak signal of the detrended and filtered time series within the time window ± 75 s from the maximum pressure drop time, and S_{noise} is the noise signal—the median of the absolute value of the detrended and filtered time series within the time window -450 to -75 s (i.e., before the encounter of a convective vortex). An example of the vertical ground acceleration and the pressure data at the encounter of a convective vortex is shown in Figure 4a, and the SNR evaluations at Band 2 and Band 5 are shown in Figures 4b and 4c. Basically, the SNR gets lower as the frequency band becomes higher due to the increase of the contribution

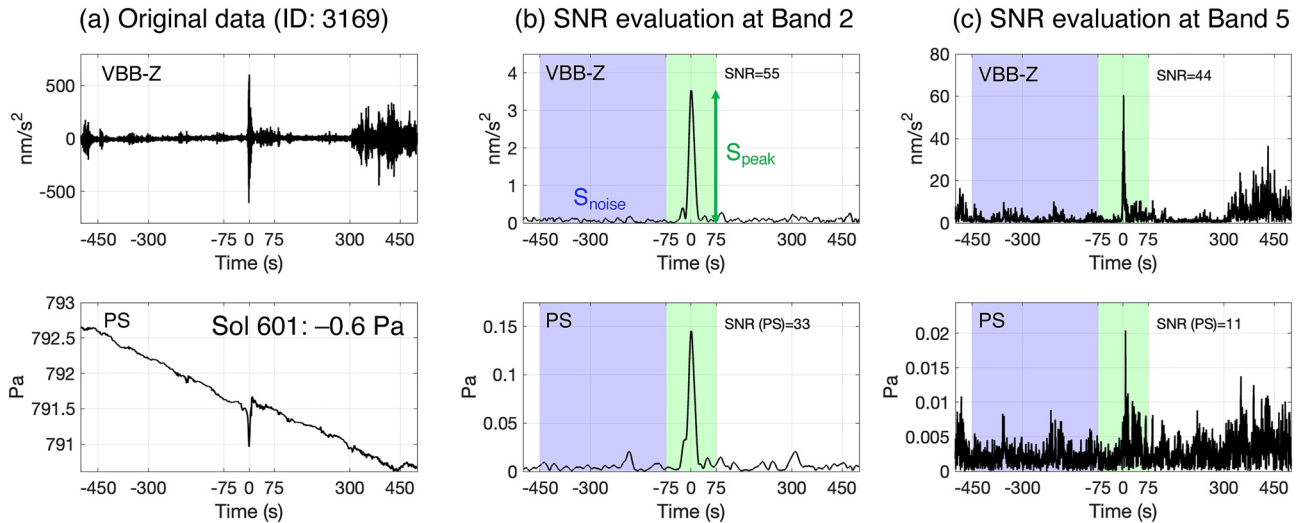


Figure 4. (a) An example of the vertical acceleration and atmospheric pressure recordings at the encounter of a vortex on Sol 601 (Event ID = 3169). The event ID is linked to our catalog. (b) Time series of the absolute value of the vertical acceleration and the atmospheric pressure filtered at Band 2 (0.05–0.1 Hz). The blue and green areas define the noise and event signals, respectively. (c) Time series of the absolute value of the vertical acceleration recorded by Very Broad-Band and the atmospheric pressure filtered at Band 5 (1.0–2.0 Hz). The blue and green areas define the noise and event signals, respectively.

from the small turbulence and/or instrumental noises. It is noteworthy that not all vortices show this trend because the excited frequency energy range differs from event to event. We confirmed that some events excite the energy at a higher frequency (>1 Hz) while others hold the energy only at a low frequency (0.05–0.1 Hz). We guess these differences might be related to the spatial scale of vortices although it is not conclusive yet. The detailed classification of the detected vortices and the quantitative discussion will be addressed in our future publications.

5.2. Ambient Wind Speed, Wind Direction, and Air Temperature

The evaluation of the ambient environment is important for understanding the vortices' advection because the vortices are considered to be transported by the ambient winds (e.g., Perrin et al., 2020; Sinclair, 1973; Spiga et al., 2021). As the wind and temperature drastically change at the encounter of the vortices with the InSight lander, we assess the ambient wind speed, wind direction, and air temperature using the 5-min time window (from -150 to -450 s) prior to each vortex encounter (Figure 5). The average and standard deviation values are stored in our catalog.

As mentioned in Section 2, the accuracies for the measurements are 1 m/s, 22.5° , and 5 K for wind speed, wind direction, and air temperature, respectively (e.g., Banfield et al., 2018; Spiga et al., 2021). Thus, in the analysis, one should keep in mind that these factors need to be taken into account depending on the individual interests and research objectives.

Figure 6 shows the histogram of each environmental factor (ambient wind speed, wind direction, and air temperature) estimated using the time window prior to the encounters of all convective vortices we used. The population shows the highest values at 9 m/s for the ambient wind speed, 135°N or 300°N for the ambient wind direction, and 240–250 K for the ambient air temperature. These results are consistent with the general trend seen in Figures 1b–1d, meaning the ambient environments were appropriately evaluated with our method. Note that the double peaks in wind direction are relevant to the seasonal variations, which had been numerically predicted before the landing (Spiga et al., 2018) and confirmed by the InSight observations as shown in Figure 2d. 300°N corresponds to “Season 5” in Figure 1a and 135°N is for other seasons.

5.3. Cross-Correlation Between Seismic and Pressure Data

To quantitatively assess the ground response to atmospheric pressure perturbations, we computed the cross-correlation coefficient (CC) between the seismic and pressure data. As reported by previous works (e.g., Garcia et al., 2020; Kenda et al., 2020), the correlation value varies depending on frequency; thereby we evaluated

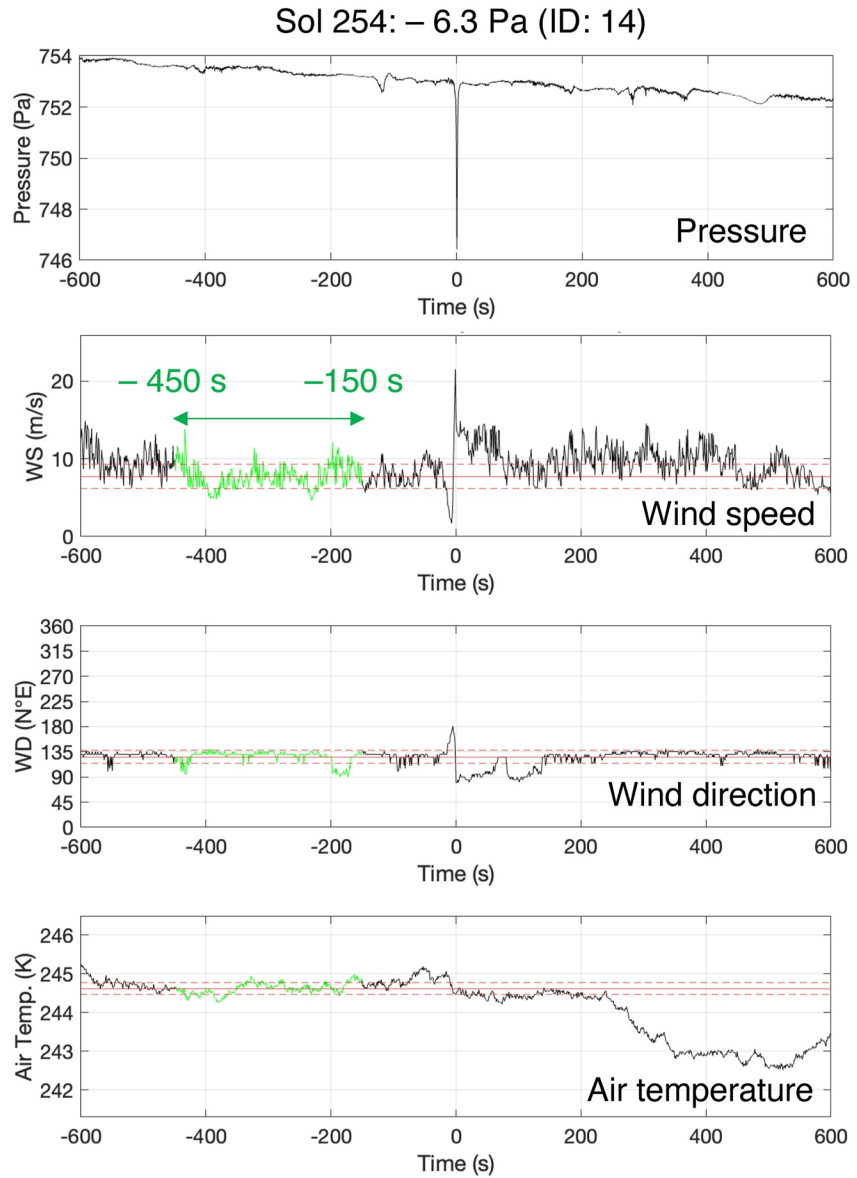


Figure 5. An example of InSight's pressure, wind, and air temperature data observed around the encounter of a vortex on Sol 254 (Event ID = 14). From top to bottom, 20 min time traces for pressure, wind speed, wind direction, and air temperature are shown (black profiles). 0 s corresponds to the maximum pressure drop time. The average (red solid line) and standard deviation (red broken lines) are computed for the time window between –150 and –450 s shown in green.

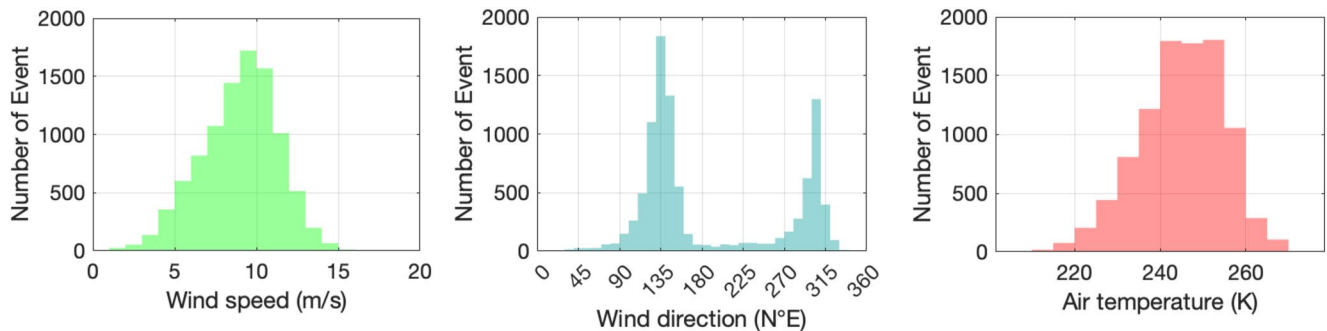


Figure 6. Histograms of the ambient wind speed (left), wind direction (middle), and air temperature (right) estimated for each vortex event in our catalog.

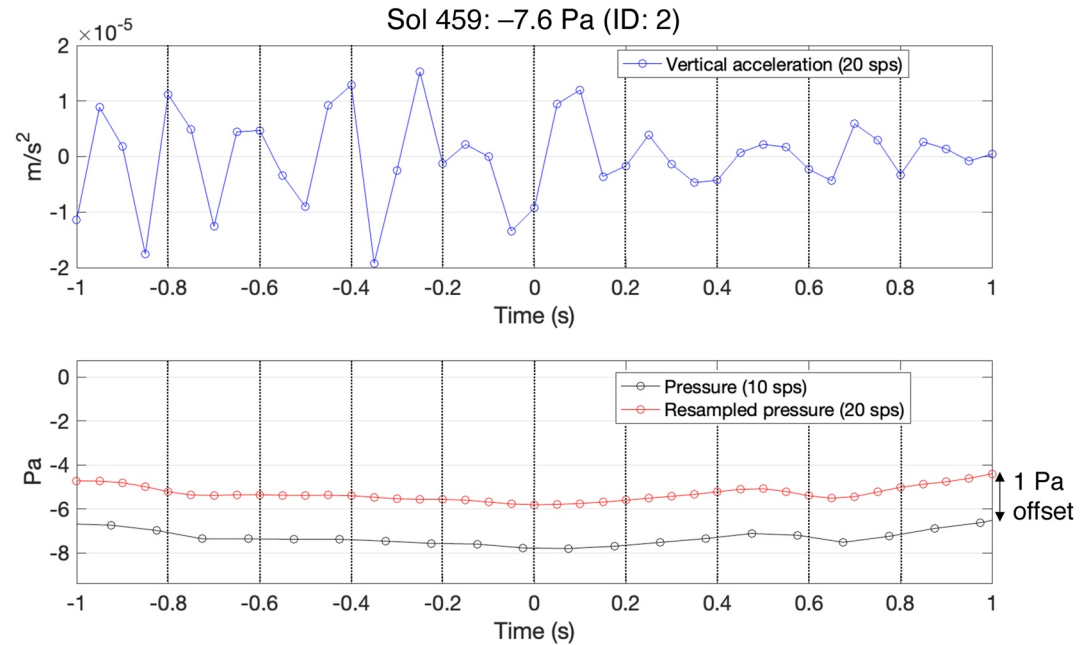


Figure 7. (top) The 20 sps vertical acceleration data around ± 1 s at the encounter of a vortex observed on Sol 459 (Event ID = 2). (bottom) the 10 sps pressure data and the resampled pressure data. The resampled signal (red) is shifted by 1 Pa to make it easier to compare with the original data (black).

it for the five frequency bands defined in Section 5.1. The processing procedure included the following steps (a) synchronizing VBB and PS data in time domain, (b) whitening (normalizing in the frequency domain) both seismic and pressure signals, and (c) computing cross-correlation between the seismic (in acceleration or velocity) and pressure data. Each process is summarized below.

First, as the pressure and seismic data were recorded at different sampling rates by individual instruments (PS: 10 sps and VBB: 20 sps), we resampled the pressure data to synchronize both time stamps. The synchronization was performed by upsampling the PS data from 10 to 80 sps in the frequency domain with zero padding. Then, the interpolation with spline fit and downsampling to 20 sps were performed in the time domain using the time stamp of the VBB data. This procedure gave us the pressure data synchronized with the seismic data (Figure 7).

Second, we performed whitening for the seismic and the resampled pressure data to make the weight of the power equal at each frequency so that the correlation coefficient does not rely on a particular frequency content. After Fourier transformation of the resampled pressure data (Figures 8a and 8b), we divided the pressure spectra with their absolute amplitude, that is, whitening (Figures 8b and 8c). Then, performing the inverse Fourier transform gave us the pressure time traces relatively enhancing phase information (Figures 8c and 8d). The same process was applied to the VBB data.

Third, the whitened seismic and pressure data were bandpass filtered with the fourth order Butterworth filter at Band 1 through Band 5, meaning that there are five pairs of time series for computing cross-correlation at various frequency ranges. An example of the filtered time traces is presented in Figures 9a and 9b. Note that the time window varies depending on the frequency to make the wavenumber consistent in each band. In this study, we defined the time window $t_{w,j}$ as:

$$t_{w,j} = 10/\overline{f_j} \quad (j = 1, 2, \dots, 5), \quad (2)$$

where $\overline{f_j}$ is the average frequency at j th frequency band. In the following, we use these processed signals for the evaluation of the correlation between ground response and pressure perturbations.

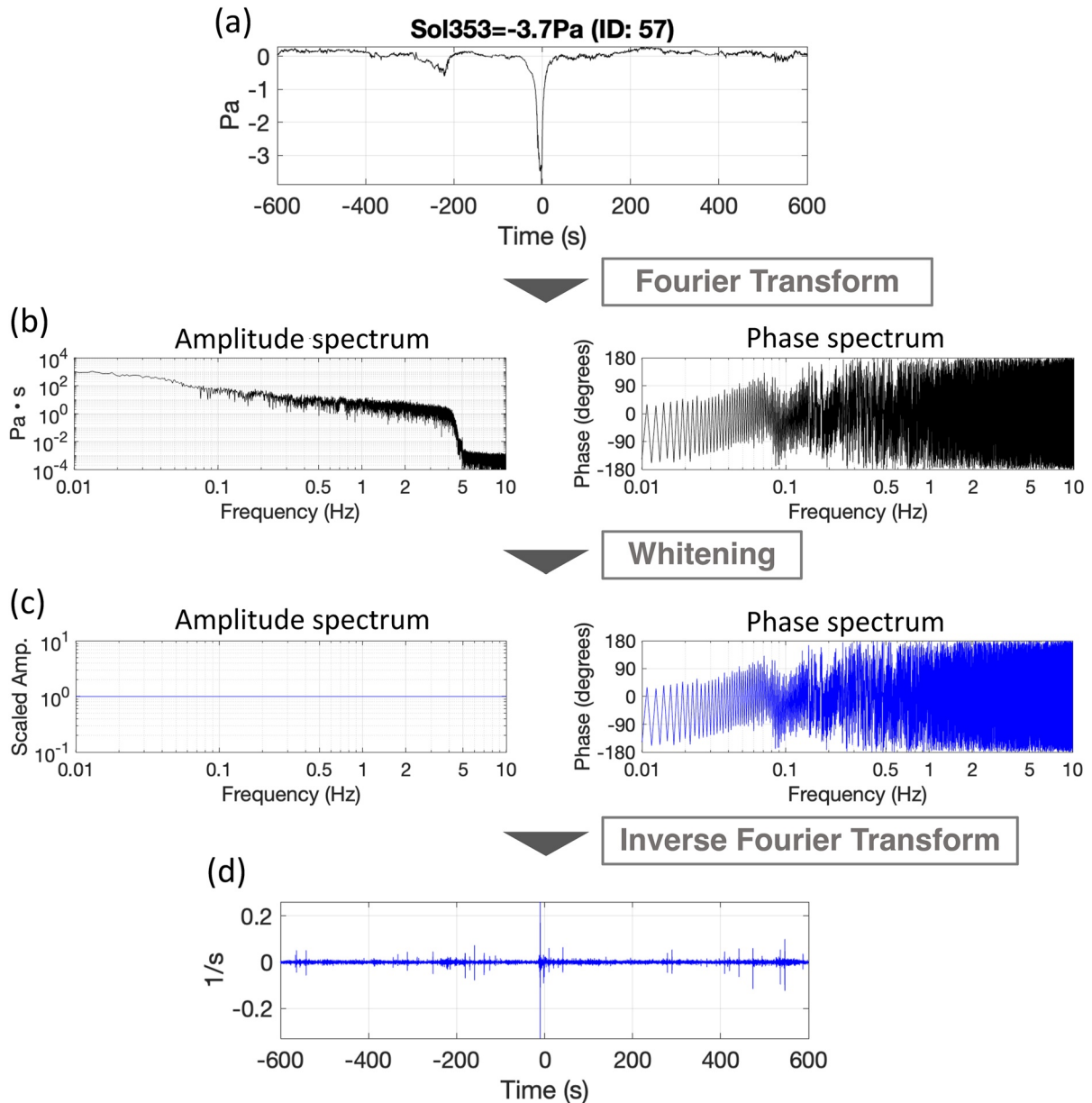


Figure 8. (a) The resampled pressure data (Event ID = 57). (b) The amplitude spectrum (left) and the phase spectrum (right) of the resampled pressure data. (c) The whitened amplitude spectrum and (left) and the phase spectrum (right). (d) The whitened pressure data (i.e., the inverse Fourier Transform of the whitened spectrum).

At the five frequency bands, we calculated the cross-correlation for the following combinations:

1. the horizontal acceleration (North or East) and the $\pi/2$ -phase shifted pressure signal,
2. the vertical acceleration and the pressure signal,
3. the horizontal velocity (North or East) and the pressure signal,
4. the vertical velocity and the $\pi/2$ -phase shifted pressure signal.

The phase shift is considered for Cases 1 and 4 assuming Sorrells' theory (e.g., Kenda et al., 2020; Sorrells, 1971). In the theory, the relation between the ground velocity and the pressure perturbation is expressed as:

$$\begin{aligned}
 v_z(\omega) &= -2ic \frac{1 - \nu^2}{E} P(\omega), \\
 v_h(\omega) &= c \frac{(1 + \nu)(1 - 2\nu)}{E} P(\omega),
 \end{aligned}
 \tag{3}$$

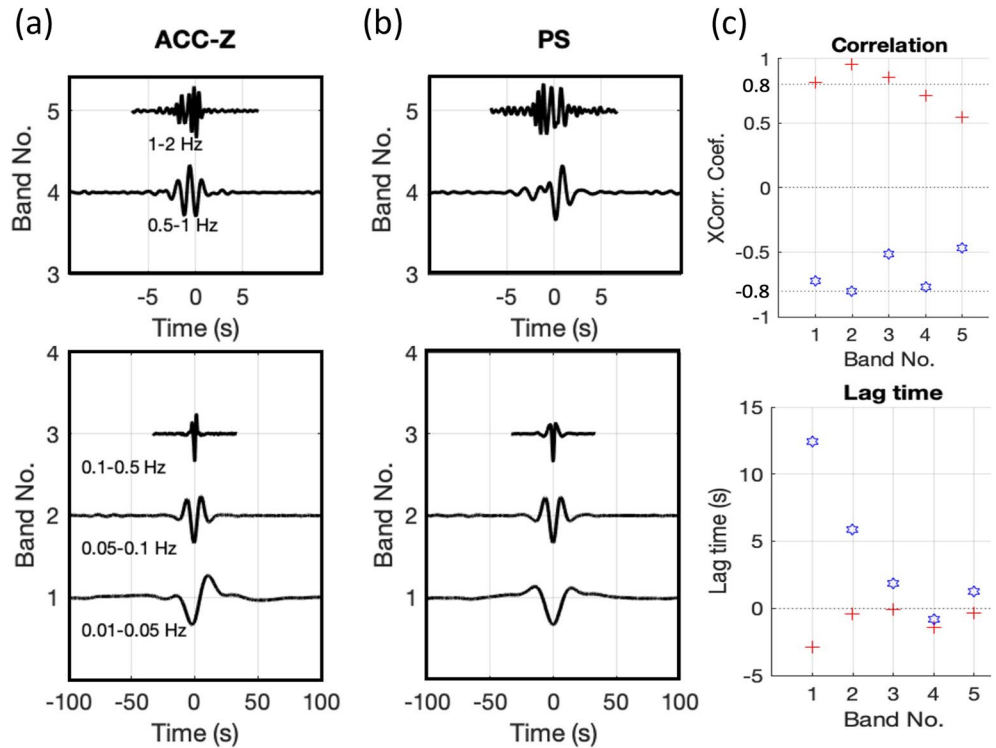


Figure 9. An example of the waveforms of (a) the vertical acceleration data and (b) the resampled pressure data filtered at various frequency bands. The waveforms filtered at Band 1–Band 3 are shown in the bottom panel and those filtered at Band 4–Band 5 are displayed in the top panel. The horizontal axis shows the time centered at the encounter of a convective vortex. (c) The maximum (red) and minimum (blue) correlation coefficients (top panel) and the lag time (bottom panel) at each frequency band. In the bottom panel, the red symbols correspond to the lag times for the maximum correlation coefficient and the blue ones correspond to those for the minimum correlation coefficient.

where v_z , v_h , P are the spectra of the vertical and horizontal ground velocities and pressure, ω is the angular frequency, c is the advection speed of a vortex—usually approximated as the ambient wind speed (e.g., Sinclair, 1973), i is the imaginary unit, ν is Poisson's ratio, and E is Young's modulus. The first expression in Equation 3 corresponds to Case 4, where $iP(\omega)$ requires the $\pi/2$ -phase shift to make the pressure signal in phase with the vertical ground velocity. It is worth noting that the conversion from the velocity to the acceleration requires a $\pi/2$ -phase shift, leading to a change in phase relation between the velocity and the pressure signal (compare Cases 1 and 3 or Cases 2 and 4). In Section 6.2, we will investigate the subsurface rigidity using this theory.

By taking the cross-correlations for the four combination cases listed above, we obtained the maximum and minimum values of the CC and the corresponding lag times at the respective frequency ranges (Figure 9c). Since the correlation coefficient helps us evaluate the quality of the atmosphere-ground coupling (e.g., Kenda et al., 2020), we can use it as a criterion for selecting the better events for the compliance analysis as discussed in Section 6.2.

5.4. Asymmetry of Pressure Drop Profiles

Looking at the pressure data, we often observe asymmetric pressure drop profiles (e.g., Figure 10a). According to Lorenz et al. (2021), these features might be related to non-uniform vortex wall structures. However, a solid conclusion to this problem has yet to be obtained. To better understand the relationship between the asymmetry and the vortex structures, we start by quantitatively evaluating the symmetry of the pressure drop profile.

In this study, we defined the asymmetry (R_{asy}) using the integral values of the left- and right-side profiles from the maximum pressure drop time. The actual process was as follows. First, we smoothed the 20 min-long detrended PS data with a 1 s time window (Figure 10a). Second, we divided the pressure profile into the left and

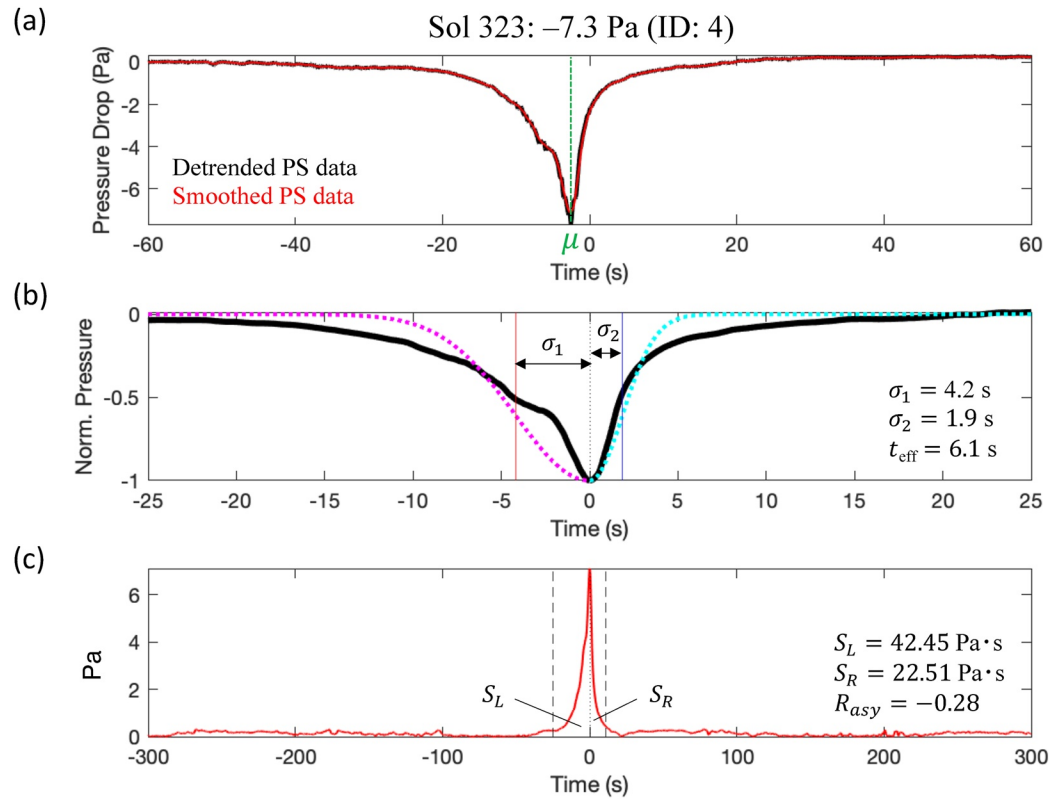


Figure 10. (a) Pressure drop signal observed on Sol 323 (Event ID = 4). The black profile is the detrended pressure data, and the red is the smoothed data with a 1 s time window. μ is the time offset parameter in Equation 4. (b) Gaussian fitting results. The black profile shows the smoothed pressure data, which is time-shifted by μ for visualization. Note that the profile is normalized by the maximum value of the absolute amplitude. The magenta and the cyan dotted lines are the Gaussian profile used for fitting the left- and right-hand profiles, respectively. (c) Pressure drop profile used for the calculation of integral values. The red curve is the pressure drop profile smoothed and converted into absolute value. The dashed vertical lines show the time interval for the integral, which is set to $6\sigma_1$ and $6\sigma_2$ from the center for the left and right sides, respectively.

right sides at the time offset parameter μ . Then, we fitted each side profile with a Half-Gaussian profile (f_{GH}) defined as:

$$f_{GH}(t) = \begin{cases} \frac{A}{\sqrt{2\pi}} \exp\left[-\frac{(t-\mu)^2}{2\sigma_1^2}\right] & (t < \mu), \\ \frac{A}{\sqrt{2\pi}} \exp\left[-\frac{(t-\mu)^2}{2\sigma_2^2}\right] & (t \geq \mu), \end{cases} \quad (4)$$

where A is a constant, t is time, σ_1 and σ_2 correspond to the half-maximum width for the left- and right-hand profiles, respectively. The event duration t_{eff} is defined as:

$$t_{eff} = \sigma_1 + \sigma_2. \quad (5)$$

Figure 10b shows an example of the best fit. Finally, the integral of both sides was performed within the time interval of $-6\sigma_1 \leq t - \mu \leq 0$ for the left side (S_L) and $0 \leq t - \mu \leq 6\sigma_2$ for the right side (S_R) (Figure 10c). The asymmetry (R_{asy}) can be defined with the integral values as:

$$R_{asy} = \log_{10}\left(\frac{S_R}{S_L}\right). \quad (6)$$

The histogram of the asymmetry is presented in Figure 11a, where $R_{asy} = 0$ means completely symmetric. Figure 11b shows a few examples of different asymmetric profiles. Here, we call the “negative” asymmetric

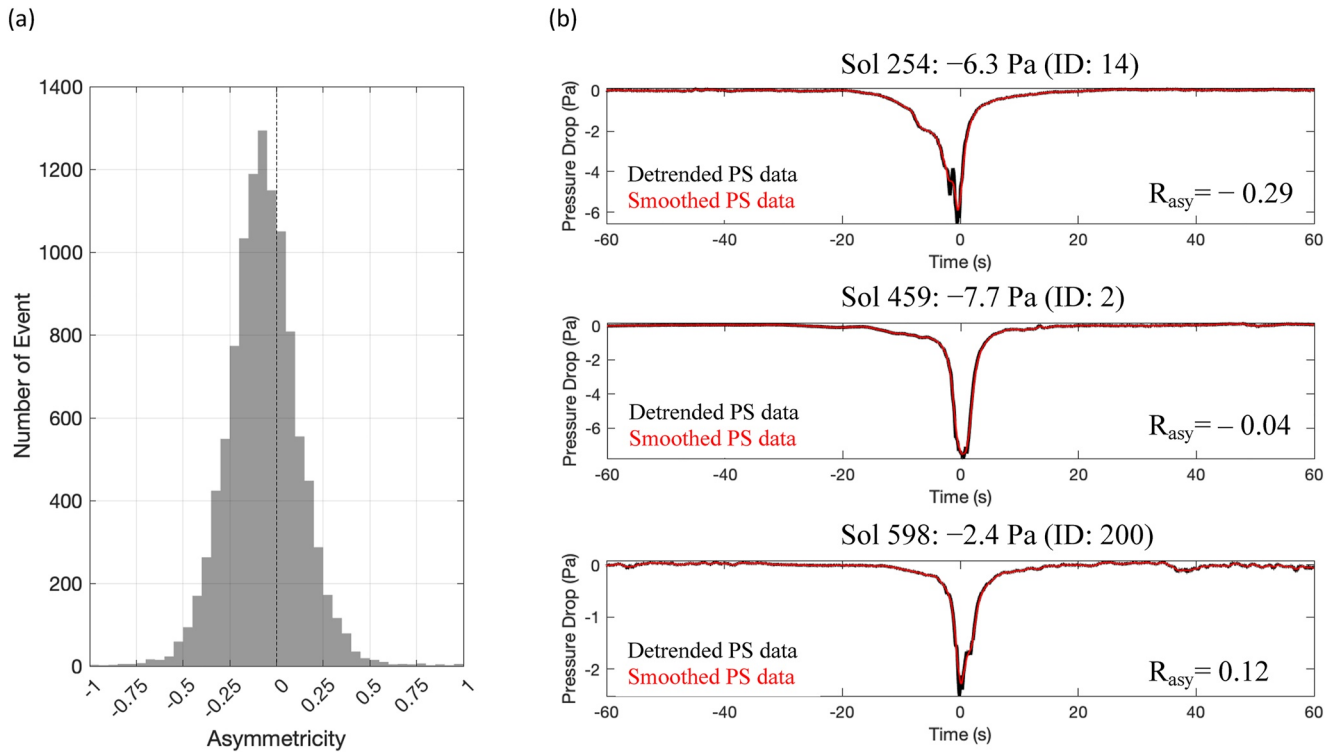


Figure 11. (a) Histogram of the asymmetry. (b) Examples of pressure drop profiles for the cases of negative asymmetric ($R_{asy} < 0$), symmetric ($R_{asy} \sim 0$), and positive asymmetric ($R_{asy} > 0$) from top to bottom.

profile when $R_{asy} < 0$ and the “positive” asymmetric profile when $R_{asy} > 0$. The histogram shows that the population reaches the peak around $R_{asy} = -0.1$, indicating the majority of events are negatively asymmetric as shown in the top panel in Figure 11b. A short discussion on this result and the relation with other parameters can be found in Section 6.1.

The evaluated parameters from Section 5.1 to Section 5.4 are compiled as a binary catalog (Onodera, 2023a). The explanation of the catalog format is summarized in Appendix A.

6. Contribution to Scientific Investigations

In this section, we demonstrate how our catalog can contribute to deepening our understanding of the Martian environment. Here we focus on two topics. One is dedicated to the meteorological interpretations of a vortex structure implied from asymmetric features seen in pressure drop profiles (Section 6.1), and the other is related to the interaction between the atmosphere and the ground, which is useful for subsurface rigidity assessments (Section 6.2).

6.1. Interpreting the Asymmetrical Feature of Pressure Drop Profiles

6.1.1. Relation Between Asymmetry and the Vortex Structures

As presented in Figure 11, we found that the majority of pressure drop events showed the negatively asymmetric feature (i.e., a gradual drop toward the maximum pressure drop and a rapid recovery after the encounter), which is consistent with the result by Lorenz et al. (2021) who also quantified the asymmetry using the large pressure drops (>0.8 Pa). This result may look unreasonable in considering the two-dimensional space, where a vortex circle moves with a constant advection speed (driven by the ambient winds). In this case, a symmetric pressure drop should always be observed at the encounter with a station. Introducing a fluctuation in the advection speed could produce asymmetric profiles. However, in such a case, the population of asymmetry would be random because we do not imagine that the advection speed changes in the same way for every event. Addi-

tionally, since the InSight landing site is located at a relatively flat area (e.g., Golombek et al., 2020), we do not expect a specific geological feature to contribute to the skewed distribution of the pressure drop asymmetry (Figure 11a).

When considering the three-dimensional system, a convective vortex (whirlwind) or dust devil can be modeled with a cylinder, where the ambient wind speed may vary with altitude (e.g., Lorenz et al., 2021; Sinclair, 1973). As speculated by Lorenz et al. (2021), when the ambient wind speed at the ground c_{grd} coincides with that at the upper part of a vortex cylinder c_{up} ($c_{grd} = c_{up}$), a symmetric pressure drop would be observed at the encounter. In the case of $c_{grd} < c_{up}$, the cylinder would be tilted in the direction of advection, resulting in a “negative” asymmetric profile. On the contrary, for $c_{grd} > c_{up}$, the cylinder should be tilted in the direction opposite to the advection direction, leading to a “positive” asymmetry. Generally speaking, the wind speed increases with altitude because the surface friction has less influence on the wind behavior at higher altitudes (e.g., Spiga et al., 2021). Additionally, the dynamic pressure is proportional to the square of wind speed. As the observations of dust devils in the terrestrial field support this idea (Sinclair, 1973), our qualitative interpretation of a skewed distribution in Figure 11a seems plausible. Further detailed discussion will be addressed in future works. Combining our results with some numerical experiments and/or comparing the terrestrial observations would help to illustrate the vortex structure better.

6.1.2. Relation Between Asymmetry and Ground Coupling

Atmosphere-ground interaction is an important aspect of a convective vortex (i.e., a moving low-pressure system) because it allows us to estimate the subsurface physical properties (Section 6.2). The quality of the coupling is usually assessed with the cross-correlation between the ground motion and the pressure variation. Through the investigation of the relations between the parameters we cataloged, we found some interesting features when making a plot of asymmetry against the CC. Here, we summarize them and introduce a question for future studies.

Figure 12 shows the scatter plots of the asymmetry and CC for different frequency bands (Band 1–Band 5). Normally, we refer to events with $CC \geq 0.8$ as “high-correlation events.” As a general characteristic, the number of high-correlation events decreases as the frequency increases because they are more easily contaminated by background noises, such as wind turbulence, at a high frequency (>1 Hz). Another notable point is that a higher correlation coefficient is obtained as the asymmetry decreases (e.g., in Bands 2 and 3 in Figure 12). This implies that a better ground coupling occurs when a pressure drop is asymmetric rather than in the ideal symmetric case. However, it has yet to be understood whether “negative” asymmetry is a necessary condition to increase atmosphere-ground coupling. This would be an interesting area for future work in order to better illustrate how the atmosphere and the ground interact with each other.

In addition to the above discussions, when comparing the low-frequency bands (Band 1–Band 3), it appears that Band 1 shows a different distribution to the other bands. It is clear that the number of high-correlation events is smaller than those of Band 2 and Band 3. We suspect that the efficiency and/or quality of the atmosphere-ground coupling changes below 0.05 Hz, which could correspond to a critical point below which the ground does not deform efficiently against an external force. Or, there may be other signals dominating at the lower frequencies. This point is briefly discussed in Section 6.2.5 although we could not reach a satisfactory explanation thus far.

6.2. Compliance Analysis and 1D Rigidity Structure at the InSight Landing Site

6.2.1. Fundamental Idea of Compliance Analysis

As briefly mentioned in Section 5.3, Sorrells (1971) formulated the relation between pressure load and vertical ground velocity for a homogeneous half-space structure as Equation 3 through the seismic and meteorological observations on Earth. The compliance can be defined by taking the spectral ratio between the ground velocity and pressure:

$$\begin{aligned} \kappa_v &= \frac{|v_z(\omega)|}{|-iP(\omega)|} = 2c \frac{1 - \nu^2}{E}, \\ \kappa_h &= \frac{|v_h(\omega)|}{|P(\omega)|} = c \frac{(1 + \nu)(1 - 2\nu)}{E}, \end{aligned} \quad (7)$$

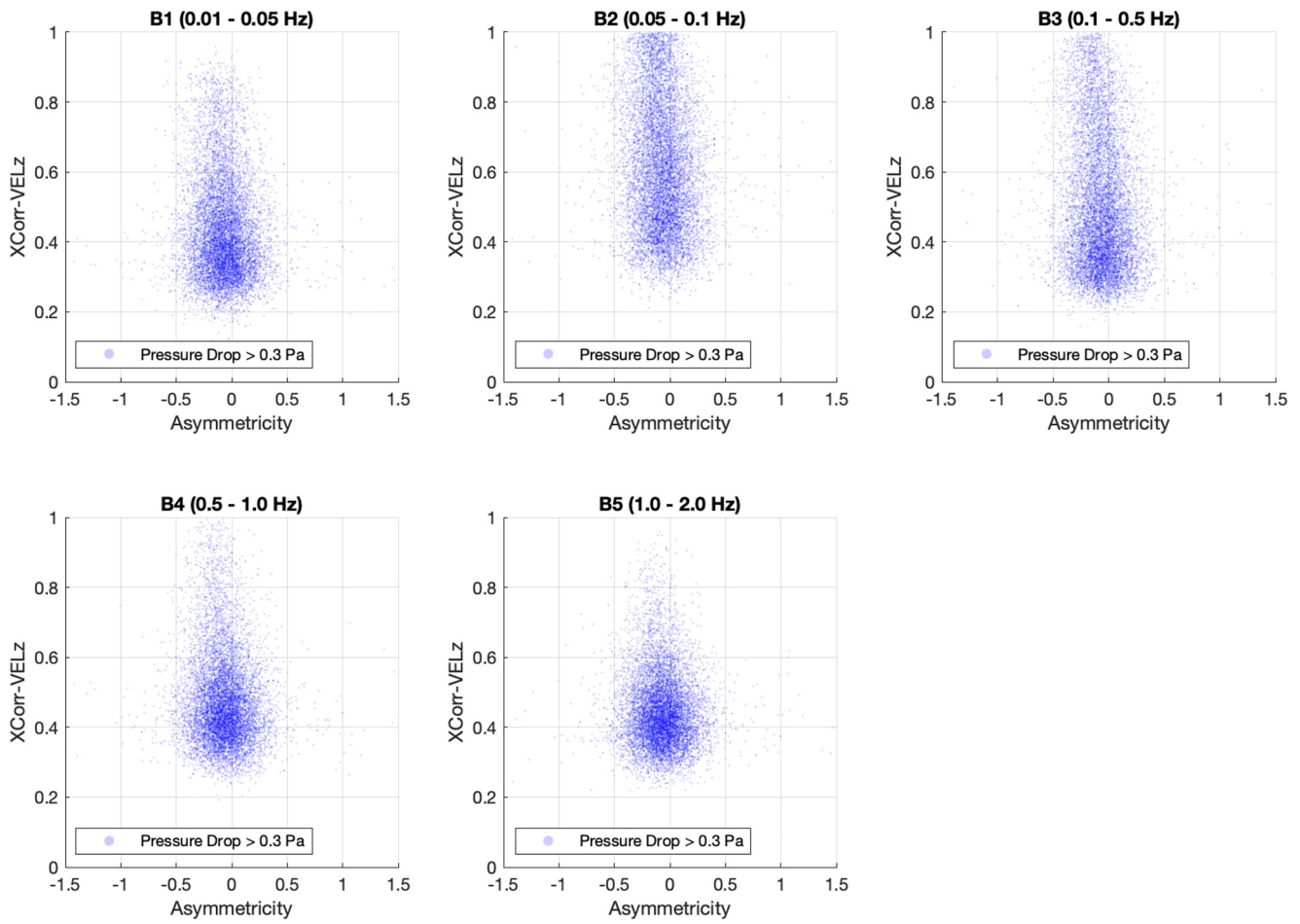


Figure 12. Scatter plots of cross-correlation coefficient against asymmetry between the vertical ground velocity and the pressure data at five frequency bands.

where κ_v and κ_h are called vertical compliance and horizontal compliance, respectively. The basic idea is to retrieve the subsurface rigidity structure by inverting the compliance profile. In this study, following Kenda et al. (2020), we use the normalized compliance ($\overline{\kappa}_v$ and $\overline{\kappa}_h$) defined as follows:

$$\begin{aligned} \overline{\kappa}_v &= 2 \frac{1 - \nu^2}{E}, \\ \overline{\kappa}_h &= \frac{(1 + \nu)(1 - 2\nu)}{E}. \end{aligned} \quad (8)$$

In the case of the horizontal component, there is an apparent effect (i.e., tilt effect) caused by the ground deformation. Generally, it is difficult to distinguish the horizontal compliance from the tilt effect without knowing the vortex trajectory. Here, we focus on the vertical component of the normalized compliance ($\overline{\kappa}_v$) in the subsequent analysis.

It is worth noting that Equations 7 and 8 are valid only for a homogeneous half-space structure. When considering a potentially stratified half space like this study, one can use the Thomson-Haskell propagator method (Haskell, 1953; Thomson, 1950) as demonstrated in Sorrells and Goforth (1973) and Kenda et al. (2020).

In solving the inversion problem, we employed almost the same approach performed by Kenda et al. (2020)—Bayesian inversion based on the Markov chain Monte Carlo (MCMC) algorithm. The main differences from their analysis are: (a) the data set covering the longer observation period is used and (b) the inversions were conducted for different wind speed groups, which allows us to retrieve different depth information. As for the first point, while Kenda et al. (2020) had analyzed the data up to Sol 227, we used the data up to Sol 900, which increased the number of available events for analysis by a factor of 10. Regarding the second point, assuming the vortices are

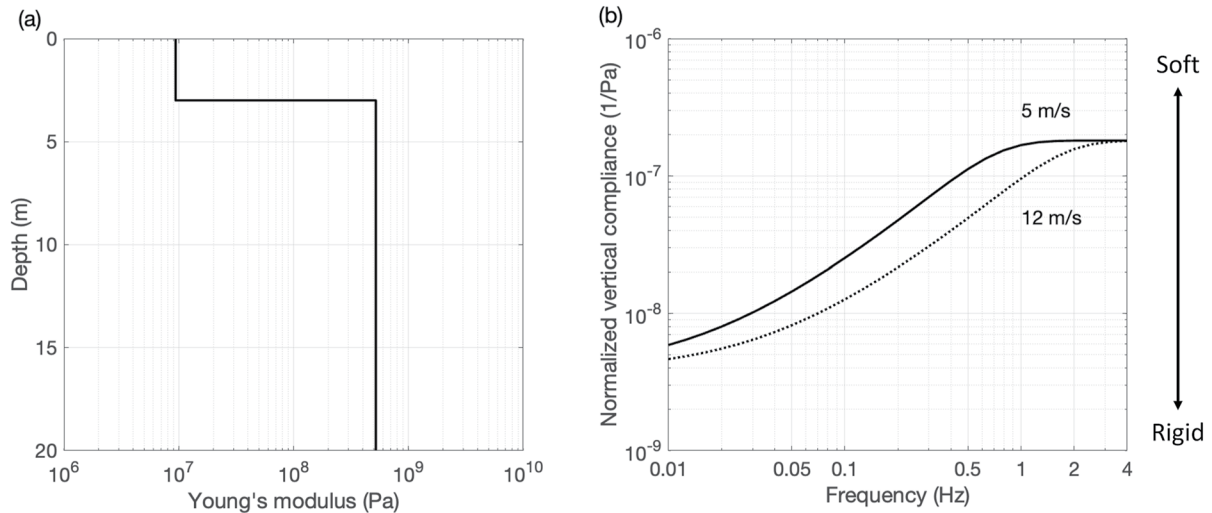


Figure 13. (a) Rigidity structure model for a demonstration. (b) Synthetic vertical compliance for different advection speeds (i.e., ambient wind speeds). The compliance is normalized by each advection speed, called normalized compliance. The solid line shows the compliance for the case of ambient wind speed of 5 m/s, and the dotted line does that for the 12 m/s case.

transported by the ambient wind c , we divided the two groups based on the histogram shown in Figure 5b—WS1 ($3.8 < c \leq 8.5$ m/s) and WS2 ($8.5 < c < 16$ m/s). Since c is related to the spatial resolution (or wavelength) in the compliance analysis, different compliance profiles can be obtained depending on the value of c for a certain rigidity structure model. Figure 13 gives an example, where the cases of $c = 5$ and 12 m/s are compared. Looking at the theoretical curves in Figure 13b, a smaller c value returns a higher normalized compliance, meaning that a smaller c is more sensitive to the shallower subsurface structure. Thus, in the following inversion, we try to retrieve different depth information by analyzing WS1 and WS2 separately.

6.2.2. Data Selection

Sorrells' theory is applicable only when the ground is well coupled with the atmosphere. To select such events, we referred to the cross-correlation coefficients (CC) calculated in Section 5.3. For the five frequency bands defined in Section 5.1, we selected the high-correlation events ($CC \geq 0.8$) and used them to compute a 2-D probability map of the normalized vertical compliance ($\overline{\kappa}_v = |v_z(\omega)|/c|P(\omega)|$). If an event shows a high correlation in Bands 2 and 3, only the normalized compliance in these bands is taken into account for the following analysis. Using the normalized compliance profiles for high-correlation events, we made 2-D probability density maps for WS1 and WS2, respectively (Figure 14). Note that there are not necessarily the same number of events in the

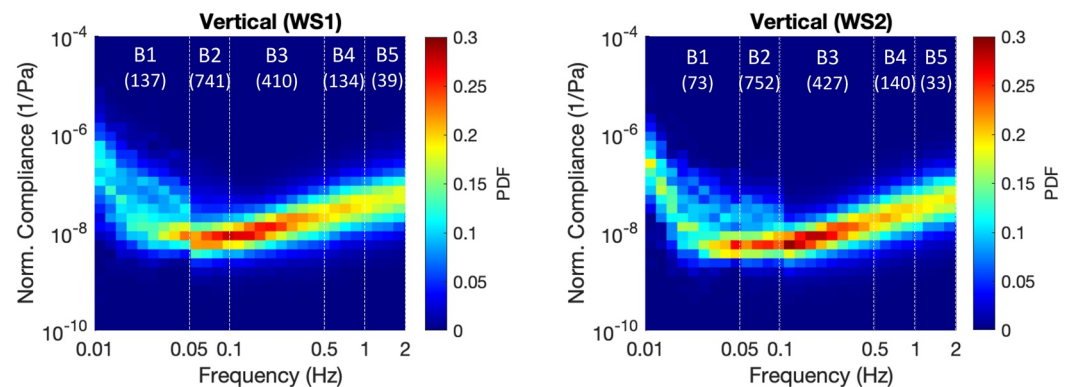


Figure 14. The observed “normalized vertical compliance” for WS1 (left) and WS2 (right). The horizontal axis shows frequency and the vertical shows the compliance normalized with ambient wind speed. The color map represents the probability density. The hotter color indicates a higher probability. White texts at the top denote the corresponding frequency bands and the number of events used for making the probability density map.

respective bands because the pressure signals correlate with those of the ground velocity differently from event to event. For example, some events show a high correlation in Band 2 and Band 3, others show from Band 3 to Band 5. From Figure 14, we can observe that there are more numbers of high-correlation events in Bands 2–3 (400–750 events), implying that these bands might be a sweet spot for the atmosphere-ground coupling caused by convective vortices. In the following inversion, we paid particular attention to Bands 2 and 3—a similar frequency band used by Kenda et al. (2020) (0.02–0.3 Hz)—because of the larger number of events and the higher probability (~30%).

6.2.3. Bayesian Inversion

For the inversions, we took the median of all the selected compliance profiles for Bands 2–3 and smoothed them over 10 data points. The error range was evaluated with the standard deviation of all the selected compliance profiles. In Figures 15a and 15b, the thick black profiles correspond to the median profiles, and the thin curves illustrate the error range for WS1 and WS2, respectively.

In the inverse problem, the vertically varying structures of Young's modulus and Poisson's ratio are retrieved by fitting the observed compliance profiles (Figures 15a and 15b). Since this problem is ill-posed, various structure models can match the observation within its error range; in other words, we cannot determine the structure uniquely. Thus, we employed a Bayesian approach to statistically assess the resultant structure and its uncertainty. Following Kenda et al. (2020), the inversion was carried out with a MCMC method (e.g., Mosegaard & Tarantola, 1995; Tarantola, 2004). Because this approach has been applied to other InSight-related works (e.g., Banerdt et al., 2020; Lognonné et al., 2020) and described by Kenda et al. (2020), here we only explain the main points.

The structures that fit the observations within the error range were searched out of prior distribution. The prior distribution defines a possible parameter range for the varying parameters, allowing us to get the physically possible solutions. For eight layers structure model, the layer's thickness, Young's modulus, and Poisson's ratio were varied in the range of 0–200 m, 10^6 – 10^{12} Pa, and 0.05–0.45, respectively. The number of layers was determined iteratively by Kenda et al. (2020). They found that eight layers were the minimum requirement to discuss the meter-scale structure for the inversion problem of compliance. For every calculation step, the synthetic normalized compliance was computed for a given structure model within the prior distribution, then we evaluated misfit (L) defined as:

$$L = \sum_N \frac{|\log_{10} C^{obs} - \log_{10} C^{calc}|}{\log_{10} \sigma}, \quad (9)$$

where C^{obs} is the observed normalized compliance, C^{calc} is the synthetic normalized compliance, and σ is the uncertainty of the observation. N refers to the grid number in the frequency domain. To get a robust result (i.e., to minimize the influence of outliers), the misfit was evaluated on a logarithmic scale. Once a model is accepted (i.e., the synthetic curve fits the observation within the error range), other structure models are tried by giving fluctuations to the previously accepted model. Additionally, to avoid the local minima, after providing some fluctuations, the input structure model is forced to vary randomly so that we can search for all possible solutions. In the end, we obtain the acceptable structure models for WS1 and WS2 as probability distributions as shown in Figures 15c and 15d. Some of the structure models to make the probability distribution maps are presented in Figures 15e and 15f. The corresponding synthetic compliance profiles are shown as the color map in Figures 15a and 15b. Since the Poisson ratio does not greatly impact the compliance curve (Kenda et al., 2020), we mainly focus on Young's modulus in the following section.

6.2.4. Estimated Subsurface Rigidity at the InSight Landing Site

The posterior probability distributions of Young's modulus for different wind speed groups are displayed in Figures 15c and 15d. Both results suggest that the InSight landing site is composed of two layers. The first layer has Young's modulus of $(0.5 - 2) \times 10^8$ Pa with 5–20 m thickness and the second layer has Young's modulus of $(0.3 - 2) \times 10^9$ Pa. According to previous works (e.g., Delage et al., 2017; Golombek et al., 2017; Morgan et al., 2018), Young's modulus of regolith is in the order of 10^7 Pa in magnitude, coarse ejecta layer takes the value of around 10^8 Pa, and fractured bedrock shows 10^{10} Pa. Comparing these values, the first layer we identified corresponds to the coarse ejecta and the second corresponds to more consolidated

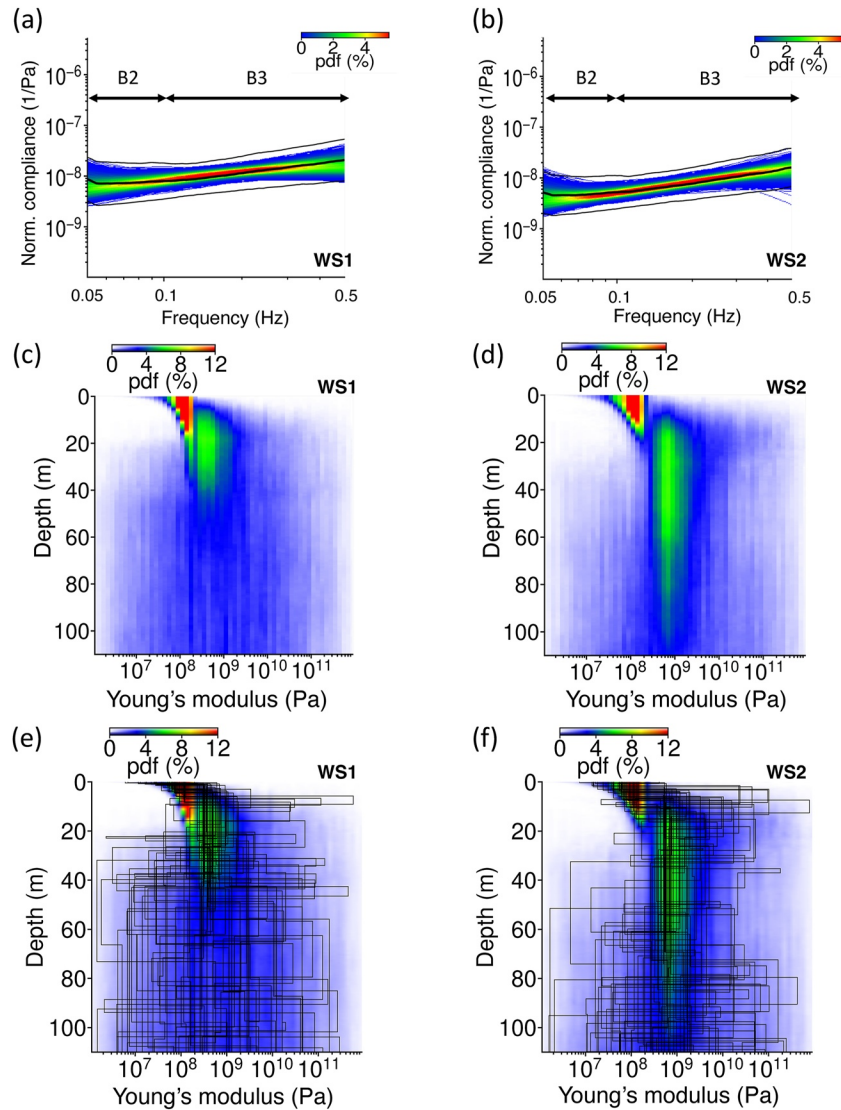


Figure 15. (a, b) Bayesian inversion results using Band 2 and Band 3 for WS1 and WS2. The horizontal axis shows frequency and the vertical axis shows the normalized compliance. The thick black lines are the median of the probability density map shown in Figure 14, and the thin black lines display the standard deviation of the probability density map shown in Figure 14. The color map indicates the probability density distribution of the fitting of the theoretical curve to the observation. (c, d) The probability density of the subsurface rigidity structure obtained through the inversion for WS1 and WS2, respectively. The horizontal axis shows Young's modulus and the vertical axis shows the depth. The hotter color indicates a higher probability. (e, f) Some structure models tried in the Bayesian inversion are superposed on the probability density maps shown in panels (c, d).

materials. Because InSight landed on the degraded crater filled with fine sand, the relatively low Young's value is expected. Our results seem consistent with the general observations at the landing site. In fact, Kenda et al. (2020), who performed a compliance analysis, also obtained a similar structure to ours down to 20 m depth.

The difference between WS1 and WS2 can be found at (a) the transition depth from the first layer to the second layer and (b) the depth extent of the second layer. Regarding the transition depth, WS1 has a smaller wind speed, and its compliance is more sensitive to the shallower part than that of WS2. Therefore, we have a higher degree of confidence in the WS1 result and interpret that the transition from the coarse ejecta to a

more consolidated layer occurs around 5–15 m deep, which looks consistent with the subsurface structure model proposed by Warner et al. (2022) who constructed the subsurface structure model based on both in situ and orbital geological observations. It is worth noting that the higher frequency contents in the compliance profile also help us to better resolve the shallower structure; thereby, applying Sorrells' theory to higher frequency bands such as Bands 4–5 would be useful for further investigation. This point is discussed in Section 6.2.5.

Concerning the deeper part, WS2 is more sensitive than WS1, and we consider that the second layer can extend down to 100 m depth. Together with the above discussion, the subsurface rigidity structure at the InSight landing site can be modeled with two layers. The structure consists of the coarse ejecta down to 5–15 m depth and gets more consolidated below that depth, extending down to 100 m. Although a previous seismological study (e.g., Hobiger et al., 2021) indicates the presence of a low rigidity layer ($\sim 10^7$ Pa) at 30–75 m, there is no strong evidence of such a layer at the corresponding depth (30–75 m) around the InSight landing site or Elysium Planitia from either geological observations or compliance analyses (e.g., Kenda et al., 2020; Warner et al., 2022). Looking at Figure 15f, while a higher probability is obtained around 10^9 Pa at a depth of 30–75 m, some low rigidity values ($\sim 10^7$ Pa) seem acceptable (bluish area). However, the model including such low rigidity values at 30–75 m returns the compliance away from the median profile of the observation (compare blue profiles and thick black line in Figure 15d). Therefore, like Warner et al. (2022) and Kenda et al. (2020), our results prefer simpler structure and do not positively support the presence of a low rigidity layer indicated by some seismological analyses (e.g., Hobiger et al., 2021).

6.2.5. Implications for Further Extension of Compliance Analysis

For further extension of the compliance approach, we summarize some ideas in this section for the following studies. Going back to Figure 14, we found that Band 1 shows significantly different behavior compared to the others. Considering that an unreasonably low-rigidity layer ($\sim 10^6$ Pa) shows up at several tens of meters deep if we include Band 1 in the inversion (Figure B1 in Appendix B), Sorrells' theory might not be applicable to this frequency band. In fact, since Sorrells (1971) assumes a plane wave for compliance analysis, the theory may not work at the lower frequency where the influence of the vortex curvature gets dominant. As another possibility, as seen on Earth, the Newtonian attraction related to the pressure perturbations could affect the seismic observations (Van Camp et al., 2017; Zürn & Wielandt, 2007). However, we found that its effect was much smaller (10 times at least) than the ground compliance at 0.01–0.05 Hz (Appendix C and Figure C1). Thus, we have not yet found a reasonable explanation for the compliance behavior in Band 1. Given these indications, one should avoid using Band 1 until the physical mechanism at the very low frequency (< 0.05 Hz) is understood. In our future work, the applicability of Sorrells' theory to the very low frequency (< 0.05 Hz) will be discussed.

On the other hand, it might be possible to apply Sorrells' theory to higher frequencies (> 0.5 Hz). Unlike Band 1, the probability density of compliance in Bands 4 and 5 is as stable as in Bands 2 and 3, and shows good continuity between each band. We think these events are helpful in resolving the shallow structures better even though there are a smaller number of events compared to Band 2 and 3. We guess the reason for their smaller population is that they are relatively small convective vortices. Smaller vortices are more easily affected by local turbulence and gain more noise, decreasing the correlation between pressure variations and ground motions. This leads to a smaller number of events available for compliance analysis. However, once a vortex structure becomes stable enough against shear forces by turbulence and is close enough to an observation point, a better atmosphere-ground coupling can be observed. To test our hypothesis, we will look closer at the higher frequency part—which can help us extract the uppermost structures (a few meter depth).

7. Concluding Remarks

For the purpose of providing useful information for the studies on the Martian atmosphere and subsurface structure, we quantitatively characterized 12,569 convective vortices observed by InSight from both meteorological and seismological aspects. The evaluated parameters (e.g., event time, pressure deficit, event duration, asymmetry, and CC between pressure variation and ground motion) are compiled as a catalog that is available online (Onodera, 2023a).

As examples of scientific applications, we investigated the asymmetry of pressure drop profiles. Some discussions led to the idea that asymmetry is related to the vortex wall structure rather than a two-dimensional advection pattern. We expect future studies will investigate our hypothesis through numerical experiments. Additionally, using events that show a high correlation between pressure and seismic (ground motion) data, we performed a compliance analysis and estimated the subsurface rigidity at the InSight landing site down to a depth of ~ 100 m. Our results suggest that the subsurface structure can be modeled with two layers: a coarse ejecta layer ($\sim 10^8$ Pa) and a more consolidated layer ($\sim 10^9$ Pa). It is indicated that the transition from the first layer to the second occurs at 5–15 m depth, which is consistent with previously proposed models (e.g., Kenda et al., 2020; Warner et al., 2022). It is worth noting that this value could be refined by including the high-frequency content in the compliance analysis because it is more sensitive to shallower depths (< 5 m).

Together with some results and discussions in this paper, our catalog will help improve our knowledge of the Martian convective vortices, atmosphere-ground interaction, and subsurface properties.

Appendix A: Catalog Format

All the previously presented data and parameters are gathered in a catalog. The catalog is available in pickle format—a binary format produced by pandas module of python—at Onodera (2023a). To read a pickle file, readers can use the following lines:

```
import pandas as pd

data = pd.read_pickle("path to pickle file")
```

By choosing the parameter name listed in Tables A1 and A2, readers can retrieve parameters depending on their interests. For example, one can get the list of all pressure drop values by running the line below:

```
param=data.PressD
```

Table A1

List of Parameter Names Related to Event ID, Detection Time, Pressure Drop Values, Ambient Factors, and Signal-To-Noise Ratio in Our Catalog

Name	Unit	Description	References
ID	–	The number is allocated from the largest pressure drop event to the smaller ones	Spiga et al. (2021)
Sol	–	InSight sol (Martian day)	Spiga et al. (2021)
LTST_h	hr	Local True Solar Time in hours at the maximum pressure drop	Spiga et al. (2021)
UTC	YYYY-DOYThh:mm:ss	Corresponding UTC of LTST_h	Spiga et al. (2021)
PressD	Pa	Value of the minimum pressure during the encounter of a vortex	Spiga et al. (2021)
Ave_WS	m/s	Average wind speed	Section 5.2
std_WS	m/s	Standard deviation of wind speed	Section 5.2
Ave_Wdir	N°E	Average wind direction	Section 5.2
std_Wdir	N°E	Standard deviation of wind direction	Section 5.2
Ave_AT	K	Average air temperature	Section 5.2
std_AT	K	Standard deviation of air temperature	Section 5.2
SNR_ACCZ_BX	–	The signal-to-noise ratio of the vertical acceleration recorded by VBB at Band X ($X = 1, 2, \dots, 5$)	Section 5.1
SNR_ACCN_BX	–	The signal-to-noise ratio of the north acceleration recorded by VBB at Band X ($X = 1, 2, \dots, 5$)	Section 5.1
SNR_ACCE_BX	–	The signal-to-noise ratio of the east acceleration recorded by VBB at Band X ($X = 1, 2, \dots, 5$)	Section 5.1
SNR_PS_BX	–	The signal-to-noise ratio of the pressure signal recorded by PS at Band X ($X = 1, 2, \dots, 5$)	Section 5.1

Table A2
List of Parameter Names Related to Cross-Correlation and Asymmetry in Our Catalog

Name	Unit	Description	References
XCC_max_VELZ_BX	–	The maximum value of the cross-correlation coefficient between the vertical velocity (VBB-Z) and phase-shifted pressure data (PS) at Band X ($X = 1, 2, \dots, 5$)	Section 5.3
XCC_max_VELN_BX	–	The maximum value of the cross-correlation coefficient between the north velocity (VBB-N) and pressure data (PS) at Band X ($X = 1, 2, \dots, 5$)	Section 5.3
XCC_max_VELE_BX	–	The maximum value of the cross-correlation coefficient between the east velocity (VBB-E) and pressure data (PS) at Band X ($X = 1, 2, \dots, 5$)	Section 5.3
XCC_min_VELZ_BX	–	The minimum value of the cross-correlation coefficient between the vertical velocity (VBB-Z) and phase-shifted pressure data (PS) at Band X ($X = 1, 2, \dots, 5$)	Section 5.3
XCC_min_VELN_BX	–	The minimum value of the cross-correlation coefficient between the north velocity (VBB-N) and pressure data (PS) at Band X ($X = 1, 2, \dots, 5$)	Section 5.3
XCC_min_VELE_BX	–	The minimum value of the cross-correlation coefficient between the east velocity (VBB-E) and pressure data (PS) at Band X ($X = 1, 2, \dots, 5$)	Section 5.3
XCC_max_ACCZ_BX	–	The maximum value of the cross-correlation coefficient between the vertical acceleration (VBB-Z) and pressure data (PS) at Band X ($X = 1, 2, \dots, 5$)	Section 5.3
XCC_max_ACCN_BX	–	The maximum value of the cross-correlation coefficient between the north acceleration (VBB-N) and phase-shifted pressure data (PS) at Band X ($X = 1, 2, \dots, 5$)	Section 5.3
XCC_max_ACCE_BX	–	The maximum value of the cross-correlation coefficient between the east acceleration (VBB-E) and phase-shifted pressure data (PS) at Band X ($X = 1, 2, \dots, 5$)	Section 5.3
XCC_min_ACCZ_BX	–	The minimum value of the cross-correlation coefficient between the vertical acceleration (VBB-Z) and pressure data (PS) at Band X ($X = 1, 2, \dots, 5$)	Section 5.3
XCC_min_ACCN_BX	–	The minimum value of the cross-correlation coefficient between the north acceleration (VBB-N) and phase-shifted pressure data (PS) at Band X ($X = 1, 2, \dots, 5$)	Section 5.3
XCC_min_ACCE_BX	–	The minimum value of the cross-correlation coefficient between the east acceleration (VBB-E) and phase-shifted pressure data (PS) at Band X ($X = 1, 2, \dots, 5$)	Section 5.3
t_lag_max_VELZ_BX	–	The lag time for “XCC_max_VELZ_BX” ($X = 1, 2, \dots, 5$)	Section 5.3
t_lag_max_VELN_BX	–	The lag time for “XCC_max_VELN_BX” ($X = 1, 2, \dots, 5$)	Section 5.3
t_lag_max_VELE_BX	–	The lag time for “XCC_max_VELE_BX” ($X = 1, 2, \dots, 5$)	Section 5.3
t_lag_min_VELZ_BX	–	The lag time for “XCC_min_VELZ_BX” ($X = 1, 2, \dots, 5$)	Section 5.3
t_lag_min_VELN_BX	–	The lag time for “XCC_min_VELN_BX” ($X = 1, 2, \dots, 5$)	Section 5.3
t_lag_min_VELE_BX	–	The lag time for “XCC_min_VELE_BX” ($X = 1, 2, \dots, 5$)	Section 5.3
t_lag_max_ACCZ_BX	–	The lag time for “XCC_max_ACCZ_BX” ($X = 1, 2, \dots, 5$)	Section 5.3
t_lag_max_ACCN_BX	–	The lag time for “XCC_max_ACCN_BX” ($X = 1, 2, \dots, 5$)	Section 5.3
t_lag_max_ACCE_BX	–	The lag time for “XCC_max_ACCE_BX” ($X = 1, 2, \dots, 5$)	Section 5.3
t_lag_min_ACCZ_BX	–	The lag time for “XCC_min_ACCZ_BX” ($X = 1, 2, \dots, 5$)	Section 5.3
t_lag_min_ACCN_BX	–	The lag time for “XCC_min_ACCN_BX” ($X = 1, 2, \dots, 5$)	Section 5.3
t_lag_min_ACCE_BX	–	The lag time for “XCC_min_ACCE_BX” ($X = 1, 2, \dots, 5$)	Section 5.3
STDEV1	s	The standard deviation of the fitted pressure drop with the left-hand side Gaussian fit	Section 5.4
STDEV2	s	The standard deviation of the fitted pressure drop with the right-hand side Gaussian fit	Section 5.4
T_eff_s	s	Effective event time (i.e., the characteristic time scale of event duration), defined by STDEV1 + STDEV2	Section 5.4
Residual_GaussFit	Pa	Summation of the residual value when PS was fitted with Gaussian curve	Section 5.4
Int1	Pa·s	The integral value of the left-hand side of the pressure drop signal	Section 5.4
Int2	Pa·s	The integral value of the right-hand side of the pressure drop signal	Section 5.4
Asymmetry	–	The asymmetry of pressure drop, defined as $\log_{10}(\text{Int2}/\text{Int1})$	Section 5.4

Appendix B: Additional Inversion Result

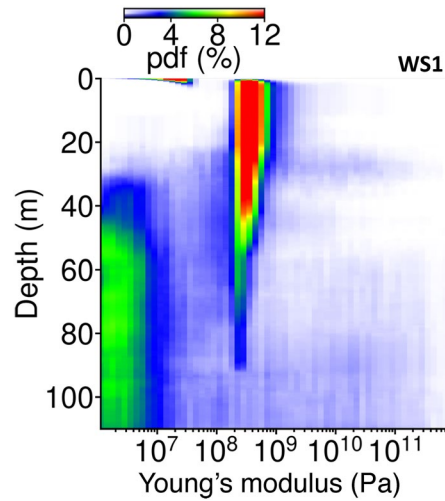


Figure B1. Probability density map for Young's modulus derived through compliance analysis (WS1) taking into account all frequency bands. There is an unreasonably soft layer ($<5 \times 10^6$ Pa) below 45 m depth which is closely related to Band 1.

Appendix C: Effect of Newtonian Attraction

It is well known that seismic observations are influenced by changes in environmental factors, one of which is the atmospheric conditions as described in this study. While this study focused on the ground deformation caused by transient pressure variations, there is another effect relevant to a change in atmospheric conditions. For example, when the air above the observation point is denser than the surrounding air, the sensor mass would be attracted toward the denser part (i.e., Newtonian attraction). According to Zürn and Wielandt (2007), the effect of Newtonian attraction becomes dominant below 2 mHz on Earth, whose intensity can be evaluated as follows:

$$\frac{\Delta g}{\Delta p} = -\frac{2\pi G}{g_0}, \tag{C1}$$

where G is gravitational constant and g_0 is the gravitational acceleration (Earth: 9.81, Mars: 3.72 m/s^2). The terrestrial value is $-4.3 \times 10^{-2} \text{ nm/s}^2/\text{Pa}$ and the Martian value is $-1.1 \times 10^{-1} \text{ (nm/s}^2/\text{Pa)}$. Figure C1 compares the

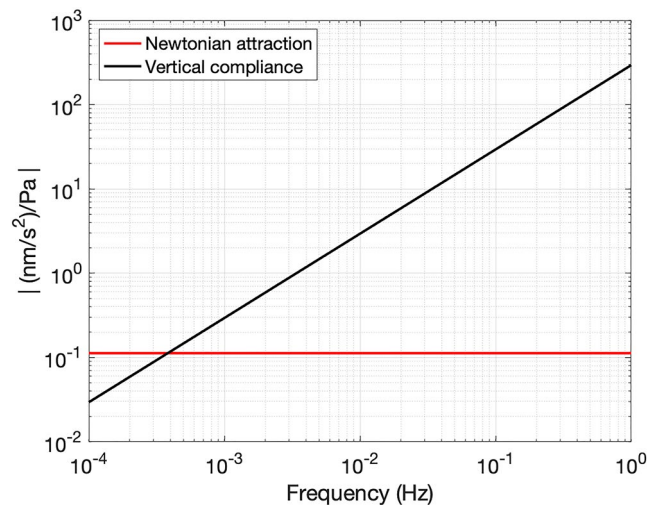


Figure C1. Comparison of the absolute intensity of Newtonian attraction and the vertical compliance. The vertical compliance was computed by multiplying 2π with Equation 7, assuming $E = 2 \times 10^8 \text{ Pa}$, $\nu = 0.25$, and $c = 5.0 \text{ m/s}$.

absolute intensity of Newtonian attraction and that of vertical compliance. At our target frequency (>0.01 Hz), Newtonian attraction is much smaller than the vertical compliance, leading to the conclusion that the unstable behavior at 0.01–0.05 Hz in Figures 15a and 15b cannot be explained with Newtonian attraction.

Data Availability Statement

The SEIS data from the InSight mission used in this study can be retrieved through InSight Mars SEIS Data Service (2019) and InSight Marsquake Service (2022). The catalog file is available at Onodera (2023a). A sample program for analyzing the VBB data can be found at Onodera (2023b).

Acknowledgments

We acknowledge NASA, CNES, their partner agencies and Institutions (UKSA, SSO, DLR, JPL, IPGP-CNRS, ETHZ, IC, and MPS- MPG), and the flight operations team at JPL, SISMOC, MSDS, IRIS-DMC, and PDS for acquiring and providing InSight data, including SEED SEIS data. This is InSight contribution number 326. K.O. is supported by JSPS KAKENHI Grant 22KJ0745. A.H. is funded by the UK Space Agency under Grant ST/R002096/1 and ST/W002523/1. M.D. was granted access to the GENCI HPC resources of IDRIS under allocation AD010413017R1. Numerical computations were partly performed on the S-CADAN/DANTE platform, IPGP, France. We would also like to show our gratitude to the editor (Dr. Laurent Montési), the associate editor (Dr. German Martínez), and two anonymous reviewers for giving us constructive advice, which made the manuscript more informative.

References

- Balme, M., & Greeley, R. (2006). Dust devils on Earth and Mars. *Reviews of Geophysics*, 44(3). <https://doi.org/10.1029/2005RG000188>
- Banerdt, W. B., Smrekar, S. E., Banfield, D., Giardini, D., Golombek, M., Johnson, C. L., et al. (2020). Initial results from the InSight mission on Mars. *Nature Geoscience*, 13(3), 183–189. <https://doi.org/10.1038/s41561-020-0544-y>
- Banfield, D. (2019). APSS PS data. *NASA Planetary Data System*. <https://doi.org/10.17189/1518939>
- Banfield, D., Rodriguez-Manfredi, J. A., Russell, C. T., Rowe, K. M., Leneman, D., Lai, H. R., et al. (2018). InSight auxiliary payload sensor suite (APSS). *Space Science Reviews*, 215(1), 4. <https://doi.org/10.1007/s11214-018-0570-x>
- Banfield, D., Spiga, A., Newman, C., Forget, F., Lemmon, M., Lorenz, R., et al. (2020). The atmosphere of Mars as observed by InSight. *Nature Geoscience*, 13(3), 190–198. <https://doi.org/10.1038/s41561-020-0534-0>
- Bila, T., Wurm, G., Onyeagusi, F. C., & Teiser, J. (2020). Lifting grains by the transient low pressure in a Martian dust devil. *Icarus*, 339, 113569. <https://doi.org/10.1016/j.icarus.2019.113569>
- Ceylan, S., Clinton, J. F., Giardini, D., Böse, M., Charalambous, C., van Driel, M., et al. (2021). Companion guide to the marsquake catalog from insight, sols 0–478: Data content and non-seismic events. *Physics of the Earth and Planetary Interiors*, 310, 106597. <https://doi.org/10.1016/j.pepi.2020.106597>
- Chatain, A., Spiga, A., Banfield, D., Forget, F., & Murdoch, N. (2021). Seasonal variability of the daytime and nighttime atmospheric turbulence experienced by insight on Mars. *Geophysical Research Letters*, 48(22), e2021GL095453. <https://doi.org/10.1029/2021GL095453>
- Clinton, J. F., Ceylan, S., van Driel, M., Giardini, D., Stähler, S. C., Böse, M., et al. (2021). The marsquake catalogue from insight, sols 0–478. *Physics of the Earth and Planetary Interiors*, 310, 106595. <https://doi.org/10.1016/j.pepi.2020.106595>
- Delage, P., Karakostas, F., Dhemaied, A., Belmokhtar, M., Lognonné, P., Golombek, M., et al. (2017). An investigation of the mechanical properties of some Martian regolith simulants with respect to the surface properties at the insight mission landing site. *Space Science Reviews*, 211(1), 191–213. <https://doi.org/10.1007/s11214-017-0339-7>
- Ellehoj, M. D., Gunnlaugsson, H. P., Taylor, P. A., Kahanpää, H., Bean, K. M., Cantor, B. A., et al. (2010). Convective vortices and dust devils at the phoenix Mars mission landing site. *Journal of Geophysical Research*, 115(E4), E00E16. <https://doi.org/10.1029/2009JE003413>
- Garcia, R. F., Kenda, B., Kawamura, T., Spiga, A., Murdoch, N., Lognonné, P. H., et al. (2020). Pressure effects on the seis-insight instrument, improvement of seismic records, and characterization of long period atmospheric waves from ground displacements. *Journal of Geophysical Research: Planets*, 125(7), e2019JE006278. <https://doi.org/10.1029/2019JE006278>
- Giardini, D., Lognonné, P., Banerdt, W. B., Pike, W. T., Christensen, U., Ceylan, S., et al. (2020). The seismicity of Mars. *Nature Geoscience*, 13(3), 205–212. <https://doi.org/10.1038/s41561-020-0539-8>
- Golombek, M., Kipp, D., Warner, N., Daubar, I. J., Ferguson, R., Kirk, R. L., et al. (2017). Selection of the insight landing site. *Space Science Reviews*, 211(1), 5–95. <https://doi.org/10.1007/s11214-016-0321-9>
- Golombek, M., Warner, N. H., Grant, J. A., Hauber, E., Ansan, V., Weitz, C. M., et al. (2020). Geology of the insight landing site on Mars. *Nature Communications*, 11(1), 1014. <https://doi.org/10.1038/s41467-020-14679-1>
- Haskell, N. A. (1953). The dispersion of surface waves on multilayered media. *Bulletin of the Seismological Society of America*, 43(1), 17–34. <https://doi.org/10.1785/BSSA0430010017>
- Hobiger, M., Hallo, M., Schmelzbach, C., Stähler, S. C., Fäh, D., Giardini, D., et al. (2021). The shallow structure of Mars at the insight landing site from inversion of ambient vibrations. *Nature Communications*, 12(1), 6756. <https://doi.org/10.1038/s41467-021-26957-7>
- Hueso, R., Newman, C. E., del Río-Gaztelurrutia, T., Munguira, A., Sánchez-Lavega, A., Toledo, D., et al. (2023). Convective vortices and dust devils detected and characterized by Mars 2020. *Journal of Geophysical Research: Planets*, 128(2), e2022JE007516. <https://doi.org/10.1029/2022JE007516>
- InSight Marsquake Service. (2022). *Mars seismic catalogue, InSight mission; V12 2022-10-01*. ETHZ, IPGP, JPL, ICL, Univ. Bristol. <https://doi.org/10.12686/A18>
- InSight Mars SEIS Data Service. (2019). *SEIS raw data, InSight mission*. IPGP, JPL, CNES, ETHZ, ICL, MPS, ISAE-Supaero, LPG, MFSC. https://doi.org/10.18715/SEIS.INSIGHT.XB_2016
- Irving, J. C. E., Lekić, V., Durán, C., Drilleau, M., Kim, D., Rivoldini, A., et al. (2023). First observations of core-transiting seismic phases on Mars. *Proceedings of the National Academy of Sciences of the United States of America*, 120(18), e2217090120. <https://doi.org/10.1073/pnas.2217090120>
- Jackson, B. (2022). Vortices and dust devils as observed by the Mars environmental dynamics analyzer instruments on board the Mars 2020 perseverance rover. *The Planetary Science Journal*, 3(20), 20. <https://doi.org/10.3847/PSJ/ac4586>
- Kahanpää, H., Newman, C., Moores, J., Zorzano, M.-P., Martín-Torres, J., Navarro, S., et al. (2016). Convective vortices and dust devils at the MSL landing site: Annual variability. *Journal of Geophysical Research: Planets*, 121(8), 1514–1549. <https://doi.org/10.1002/2016JE005027>
- Kahre, M. A., Murphy, J. R., Newman, C. E., Wilson, R. J., Cantor, B. A., Lemmon, M. T., & Wolff, M. J. (2017). The Mars dust cycle. In R. M. Haberle, R. T. Clancy, F. Forget, M. D. Smith, & R. W. Zurek (Eds.), *The atmosphere and climate of Mars* (pp. 295–337). Cambridge University Press. <https://doi.org/10.1017/9781139060172.010>
- Kenda, B., Drilleau, M., Garcia, R. F., Kawamura, T., Murdoch, N., Compaire, N., et al. (2020). Subsurface structure at the insight landing site from compliance measurements by seismic and meteorological experiments. *Journal of Geophysical Research: Planets*, 125(6), e2020JE006387. <https://doi.org/10.1029/2020JE006387>

- Kenda, B., Lognonné, P., Spiga, A., Kawamura, T., Kedar, S., Banerdt, W. B., et al. (2017). Modeling of ground deformation and shallow surface waves generated by Martian dust devils and perspectives for near-surface structure inversion. *Space Science Reviews*, 211(1), 501–524. <https://doi.org/10.1007/s11214-017-0378-0>
- Khan, A., Ceylan, S., van Driel, M., Giardini, D., Lognonné, P., Samuel, H., et al. (2021). Upper mantle structure of Mars from InSight seismic data. *Science*, 373(6553), 434–438. <https://doi.org/10.1126/science.abf2966>
- Knapmeyer-Endrun, B., Panning, M. P., Bissig, F., Joshi, R., Khan, A., Kim, D., et al. (2021). Thickness and structure of the Martian crust from InSight seismic data. *Science*, 373(6553), 438–443. <https://doi.org/10.1126/science.abf8966>
- Lognonné, P., Banerdt, W., Clinton, J., Garcia, R., Giardini, D., Knapmeyer-Endrun, B., et al. (2023). Mars seismology. *Annual Review of Earth and Planetary Sciences*, 51(1), 643–670. <https://doi.org/10.1146/annurev-earth-031621-073318>
- Lognonné, P., Banerdt, W. B., Giardini, D., Pike, W. T., Christensen, U., Laudet, P., et al. (2019). SEIS: InSight's seismic experiment for internal structure of Mars. *Space Science Reviews*, 215(1), 12. <https://doi.org/10.1007/s11214-018-0574-6>
- Lognonné, P., Banerdt, W. B., Pike, W. T., Giardini, D., Christensen, U., Garcia, R. F., et al. (2020). Constraints on the shallow elastic and anelastic structure of Mars from InSight seismic data. *Nature Geoscience*, 13(3), 213–220. <https://doi.org/10.1038/s41561-020-0536-y>
- Lorenz, R. D., Kedar, S., Murdoch, N., Lognonné, P., Kawamura, T., Mimoun, D., & Bruce Banerdt, W. (2015). Seismometer detection of dust devil vortices by ground tilt. *Bulletin of the Seismological Society of America*, 105(6), 3015–3023. <https://doi.org/10.1785/0120150133>
- Lorenz, R. D., Spiga, A., Lognonné, P., Plasman, M., Newman, C. E., & Charalambous, C. (2021). The whirlwinds of Elysium: A catalog and meteorological characteristics of “dust devil” vortices observed by InSight on Mars. *Icarus*, 355, 114119. <https://doi.org/10.1016/j.icarus.2020.114119>
- Martínez, G. M., Newman, C. N., De Vicente-Retortillo, A., Fischer, E., Renno, N. O., Richardson, M. I., et al. (2017). The modern near-surface Martian climate: A review of in-situ meteorological data from Viking to Curiosity. *Space Science Reviews*, 212(1), 295–338. <https://doi.org/10.1007/s11214-017-0360-x>
- Morgan, P., Grott, M., Knapmeyer-Endrun, B., Golombek, M., Delage, P., Lognonné, P., et al. (2018). A pre-landing assessment of regolith properties at the InSight landing site. *Space Science Reviews*, 214(6), 104. <https://doi.org/10.1007/s11214-018-0537-y>
- Mosegaard, K., & Tarantola, A. (1995). Monte Carlo sampling of solutions to inverse problems. *Journal of Geophysical Research*, 100(B7), 12431–12447. <https://doi.org/10.1029/94JB03097>
- Mueller, D., & Abu-Mulaweh, H. (2006). Prediction of the temperature in a fin cooled by natural convection and radiation. *Applied Thermal Engineering*, 26(14), 1662–1668. <https://doi.org/10.1016/j.applthermaleng.2005.11.014>
- Murdoch, N., Kenda, B., Kawamura, T., Spiga, A., Lognonné, P., Mimoun, D., & Banerdt, W. B. (2017). Estimations of the seismic pressure noise on Mars determined from large eddy simulations and demonstration of pressure decorrelation techniques for the InSight mission. *Space Science Reviews*, 211(1), 457–483. <https://doi.org/10.1007/s11214-017-0343-y>
- Murdoch, N., Spiga, A., Lorenz, R., Garcia, R. F., Perrin, C., Widmer-Schmidrig, R., et al. (2021). Constraining Martian regolith and vortex parameters from combined seismic and meteorological measurements. *Journal of Geophysical Research: Planets*, 126(2), e2020JE006410. <https://doi.org/10.1029/2020JE006410>
- Murphy, J., & Nelli, S. (2002). Mars Pathfinder convective vortices: Frequency of occurrence. *Geophysical Research Letters*, 29(23), 18–1–18–4. <https://doi.org/10.1029/2002GL015214>
- Murphy, J., Steakley, K., Balme, M., Deprez, G., Esposito, F., Kahanpää, H., et al. (2016). Field measurements of terrestrial and Martian dust devils. *Space Science Reviews*, 203(1), 39–87. <https://doi.org/10.1007/s11214-016-0283-y>
- Newman, C., Hueso, R., Lemmon, M. T., Munguira, A., Vicente-Retortillo, Á., Apestigue, V., et al. (2022). The dynamic atmospheric and Aeolian environment of Jezero crater, Mars. *Science Advances*, 8(21), eabn3783. <https://doi.org/10.1126/sciadv.abn3783>
- Onodera, K. (2023a). InSight's seismic and meteorological data related to the Martian convective vortices. *Zenodo*. <https://doi.org/10.5281/zenodo.8097631>
- Onodera, K. (2023b). Sample program for analyzing the InSight seismic data. *Zenodo*. <https://doi.org/10.5281/zenodo.7927454>
- Ordóñez-Etxeberria, I., Hueso, R., & Sánchez-Lavega, A. (2018). A systematic search of sudden pressure drops on Gale crater during two Martian years derived from MSL/REMS data. *Icarus*, 299, 308–330. <https://doi.org/10.1016/j.icarus.2017.07.032>
- Perrin, C., Rodríguez, S., Jacob, A., Lucas, A., Spiga, A., Murdoch, N., et al. (2020). Monitoring of dust devil tracks around the InSight landing site, Mars, and comparison with in situ atmospheric data. *Geophysical Research Letters*, 47(10), e2020GL087234. <https://doi.org/10.1029/2020GL087234>
- Reiss, D., Spiga, A., & Erkeling, G. (2014). The horizontal motion of dust devils on Mars derived from CRISM and CTX/HIRISE observations. *Icarus*, 227, 8–20. <https://doi.org/10.1016/j.icarus.2013.08.028>
- Rodríguez-Manfredi, J. A. (2019). APSS TWINS data. *NASA Planetary Data System*. <https://doi.org/10.17189/1518950>
- Ryan, J. A., & Lucich, R. D. (1983). Possible dust devils, vortices on Mars. *Journal of Geophysical Research*, 88(C15), 11005–11011. <https://doi.org/10.1029/JC088iC15p11005>
- Sinclair, P. C. (1973). The lower structure of dust devils. *Journal of the Atmospheric Sciences*, 30(8), 1599–1619. [https://doi.org/10.1175/1520-0469\(1973\)030<1599:TLSODD>2.0.CO;2](https://doi.org/10.1175/1520-0469(1973)030<1599:TLSODD>2.0.CO;2)
- Sorrells, G. G. (1971). A preliminary investigation into the relationship between long-period seismic noise and local fluctuations in the atmospheric pressure field. *Geophysical Journal International*, 26(1–4), 71–82. <https://doi.org/10.1111/j.1365-246X.1971.tb03383.x>
- Sorrells, G. G., & Goforth, T. T. (1973). Low-frequency earth motion generated by slowly propagating partially organized pressure fields. *Bulletin of the Seismological Society of America*, 63(5), 1583–1601. <https://doi.org/10.1785/BSSA0630051583>
- Sorrells, G. G., McDonald, J. A., Der, Z. A., & Herrin, E. (1971). Earth motion caused by local atmospheric pressure changes. *Geophysical Journal of the Royal Astronomical Society*, 26(1–4), 83–98. <https://doi.org/10.1111/j.1365-246X.1971.tb03384.x>
- Spiga, A., Banfield, D., Teanby, N. A., Forget, F., Lucas, A., Kenda, B., et al. (2018). Atmospheric science with InSight. *Space Science Reviews*, 214(7), 109. <https://doi.org/10.1007/s11214-018-0543-0>
- Spiga, A., Murdoch, N., Lorenz, R., Forget, F., Newman, C., Rodríguez, S., et al. (2021). A study of daytime convective vortices and turbulence in the Martian planetary boundary layer based on half-a-year of InSight atmospheric measurements and large-eddy simulations. *Journal of Geophysical Research: Planets*, 126(1), e2020JE006511. <https://doi.org/10.1029/2020JE006511>
- Stähler, S. C., Khan, A., Banerdt, W. B., Lognonné, P., Giardini, D., Ceylan, S., et al. (2021). Seismic detection of the Martian core. *Science*, 373(6553), 443–448. <https://doi.org/10.1126/science.abi7730>
- Tarantola, A. (2004). *Inverse problem theory and methods for model parameter estimation*. Society for Industrial and Applied Mathematics.
- Thomson, W. T. (1950). Transmission of elastic waves through a stratified solid medium. *Journal of Applied Physics*, 21(2), 89–93. <https://doi.org/10.1063/1.1699629>
- Van Camp, M., de Viron, O., Watlet, A., Meurers, B., Francis, O., & Caudron, C. (2017). Geophysics from terrestrial time-variable gravity measurements. *Reviews of Geophysics*, 55(4), 938–992. <https://doi.org/10.1002/2017RG000566>

- Warner, N. H., Golombek, M. P., Ansan, V., Marteau, E., Williams, N., Grant, J. A., et al. (2022). In situ and orbital stratigraphic characterization of the insight landing site—A type example of a regolith-covered lava plain on mars. *Journal of Geophysical Research: Planets*, 127(4), e2022JE007232. <https://doi.org/10.1029/2022JE007232>
- Zorzano, M.-P., Vázquez, L., & Jimenez, S. (2009). Retrieval of ultraviolet spectral irradiance from filtered photodiode measurements. *Inverse Problems*, 25(11), 115023. <https://doi.org/10.1088/0266-5611/25/11/115023>
- Zürn, W., & Wielandt, E. (2007). On the minimum of vertical seismic noise near 3 mHz. *Geophysical Journal International*, 168(2), 647–658. <https://doi.org/10.1111/j.1365-246X.2006.03189.x>